

Real-Time Protection of the JET ITER-like Wall based on Near Infrared Imaging Diagnostic Systems

A. Huber¹, D. Kinna², V. Huber³, G. Arnoux², G. Sergienko¹, I. Balboa², C. Balorin⁴, P. Carman², P. Carvalho⁵, S. Collins², N. Conway², P. McCullen², A. Drenik⁶, S. Jachmich⁷, M. Jouve⁴, Ch. Linsmeier¹, B. Lomanowski⁸, P. J. Lomas², C. G. Lowry^{9,10}, C.F. Maggi², G.F. Matthews², A. Meigs², Ph. Mertens¹, I. Nunes⁵, M. Price², P. Puglia¹¹, V. Riccardo², F. G. Rimini², A. Widdowson², K-D. Zastrow² and JET contributors*

EUROfusion Consortium, JET, Culham Science Centre, Abingdon, OX14 3DB, UK

¹*Forschungszentrum Jülich GmbH, Institut für Energie- und Klimaforschung – Plasmaphysik, Partner of the Trilateral Euregio Cluster (TEC), 52425 Jülich, Germany*

²*CCFE, Culham Science Centre, Abingdon, OX14 3DB, UK*

³*Forschungszentrum Jülich GmbH, Supercomputing Centre, 52425 Jülich, Germany*

⁴*CEA, IRFM, 13108 St Paul lez Durance, France*

⁵*Instituto de Plasmas e Fusão Nuclear, Instituto Superior Técnico, Universidade de Lisboa, Lisboa, Portugal*

⁶*Max-Planck-Institut für Plasmaphysik, 85748 Garching b. München, Germany*

⁷*Laboratory for Plasma Physics, ERM/KMS, B-1000 Brussels, Belgium*

⁸*Aalto University, P.O.Box 14100, FIN-00076 Aalto, Finland*

⁹*European Commission, B1049 Brussels, Belgium*

¹⁰*JET Exploitation Unit, Culham Science Centre, Abingdon OX14 3DB, UK*

¹¹*Ecole Polytechnique Fédérale de Lausanne (EPFL), Swiss Plasma Center (SPC), CH-1015 Lausanne, Switzerland*

E-mail: A.Huber@fz-juelich.de

Keywords: Imaging diagnostics, Real-Time protection system, Hot spots, JUVIL Software, Image processing

Abstract:

In JET with ITER-like wall (JET-ILW), the first wall was changed to metallic materials (tungsten and beryllium) [1] which require a reliable protection system to avoid damage of the plasma-facing components (PFCs) due to beryllium melting or cracking of tungsten owing to thermal fatigue. To address this issue, a protection system with real time control, based on imaging diagnostics, has been implemented on JET-ILW in 2011.

*See the author list of “X. Litaudon *et al* 2017 *Nucl. Fusion* 57 102001”

This paper describes the design, implementation, and operation of the near infrared imaging diagnostic system of the JET-ILW plasma experiment and its integration into the existing JET-ILW protection architecture. The imaging system comprises eleven analogue CCD cameras which demonstrate a high robustness against changes of system parameters like the emissivity. The system covers about two thirds of the main chamber wall and almost half of the divertor. A real-time imaging processing unit is used to convert the raw data into surface temperatures taking into account the different emissivity for the various materials and correcting for artefacts resulting e.g. from neutron impact. Regions of interest (ROI) on the selected PFCs are analysed in real time and the maximum temperature measured for each ROI is sent to other real time systems to trigger an appropriate response of the plasma control system, depending on the location of a hot spot.

A hot spot validation algorithm was successfully integrated into the real-time system and is now used to avoid false alarms caused by neutrons and dust. The design choices made for the video imaging system, the implications for the hardware components and the calibration procedure are discussed. It will be demonstrated that the video imaging protection system can work properly under harsh electromagnetic conditions as well as under neutron and gamma radiation. Examples will be shown of instances of hot spot detection that abort the plasma discharge. The limits of the protection system and the associated constraints on plasma operation are also presented.

The Real-Time Protection system has been operating routinely since 2011. During this period, less than 0.5% of the terminated discharges were aborted by a malfunction of the system. About 2-3% of the discharges were terminated due to the detection of actual hot spots.

1. Introduction

The plasma-facing components (PFC) in the all metal JET ITER-like wall (JET-ILW) which consists mainly of Be and W tiles, are subject to high heat fluxes which can lead to damages such as beryllium melting or thermal fatigue of tungsten. In order to safeguard the first wall of the JET-ILW machine, a protection system, based on imaging diagnostics and running in real time, was implemented on JET in 2011/2012.

The operation of the JET-ILW started in 2011 [1]. The annotated photograph of the ITER-like wall in Fig. 1 shows the material configuration of the first wall. In the high heat loaded divertor area, bulk tungsten and tungsten coatings on Carbon Fibre reinforced Carbon (CFC) substrates are used. In the main chamber wall bulk beryllium limiter tiles and beryllium coatings on Inconel alloy 625 are installed between the limiters for the main chamber wall. Tungsten coated

CFC has been used in some higher heat flux recessed areas, for example, the neutral beam shine through region. Bulk beryllium is used for the upper dump plates, the saddle coil protection

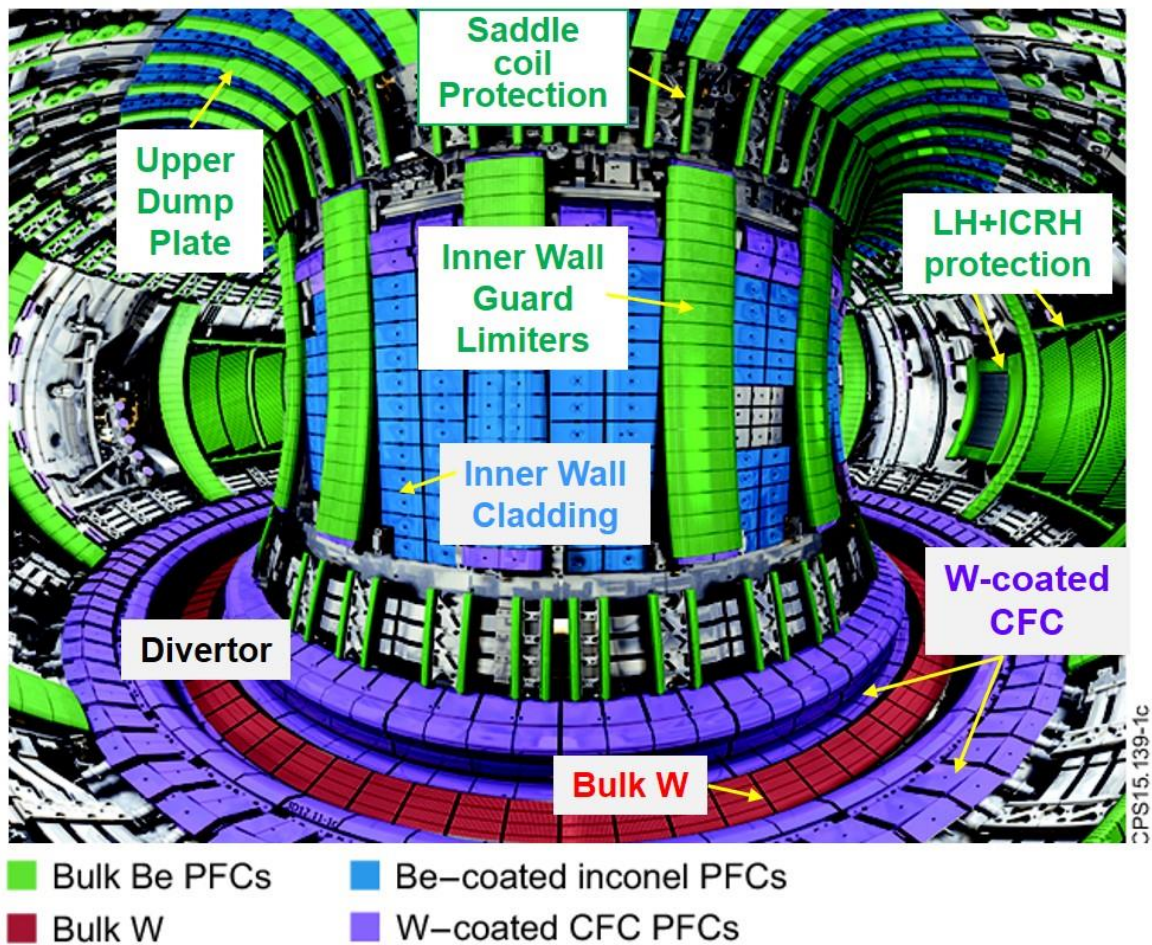


Fig.1: The JET ITER-like wall, showing the distribution of solid beryllium, beryllium-coated Inconel, solid tungsten and tungsten-coated carbon fibre composite tiles (picture adapted from [2]).

tiles (upper and lower), the antenna protection of the lower hybrid (LH) and of the ion cyclotron resonance (ICRH) heating systems.

All plasma-facing components in the ITER-like Wall are only inertially cooled. Thus, the power handling capability of the ITER-like Wall is strongly determined by the heat capacity.

With due consideration to the different materials on JET-ILW, the real time imaging system must fulfil the following objectives:

- avoid the melting of the beryllium wall components (melting point of beryllium 1287°C),
- minimize the risk of delamination of the tungsten coated tiles (the temperature should be kept below 1200°C) [3] and
- keep the surface temperature below threshold at which the bulk tungsten re-crystallizes (1200°C) [4,5].

These objectives require that the surface temperature monitoring of plasma-facing components (PFC) is considered mandatory for every plasma discharge in order to avoid overheating and eventual damage. Based on these aims, the protection cameras should deliver reliable measurements in the following operating temperature ranges for the main materials used on JET-ILW: Be 750-1400°C; W coating 750-1350°C; W 750-1400°C. In these temperature ranges, near infrared (NIR), mid-wave infrared (MWIR), as well as long-wave infrared (LWIR) cameras could be used for the temperature monitoring. The required accuracy for the surface temperature measurement defined in the JET-ILW instructions is $\pm 50^\circ\text{C}$.

The main goal of the real-time protection system is to protect bulk material components as well as the tungsten-coated tiles against overheating, especially against the formation of so-called hot spots. Hot spots are defined as localized regions on the surface of the wall tiles that have higher temperatures than the surrounding regions.

We will consider two types of overheating:

1. The increase of the surface temperature above a given value could lead to the severe damage of the wall tiles and is an important objectives for the protection:
 - The overheating of the PFCs due to heat flux overload
 - Overheating caused by fast particle losses from the NBI as well as ICRH heating. (genuine hot spots)
 - Overheating of the wall component edges due to small misalignment of components exceeding the engineering tolerances during their mounting and maintenance (genuine hot spots)
2. The surface temperature increase due to other causes than genuine overheating (false hot spots):
 - Dust particles on the surface are poorly thermally connected with the underlying material and become quickly very hot, generating false hot spots smaller than the camera resolution. A hot spot validation algorithm has been used in this case to avoid alarms caused by these false hot spots.
 - Thin surface layers can develop on the PFCs due to redeposition and lead to high-temperature hot spot formation due to their low thermal capacity and their poor thermal contact with the underlying material. The overheating of the redeposited layers does not pose a risk to the PFCs integrity but may be a cause for false alarms.
 - The delamination of the coating can lead to flakes and droplets which have a poor thermal connection to the bulk substrate and have typical dimensions $\sim 1\text{mm}$ which is below the spatial resolution of the protection system. It could produce also jagged edges of damages layers, which can receive higher heat fluxes than the original

shaped surface. Overheating of the flakes, droplets and jagged edges does not lead to a global damage of the divertor tiles, which could have an impact on the machine operation, and, therefore, the hot spots produced by delamination of the coating are considered as false hot spots.

In this overview paper we will give a technical and scientific description of the real-time protection system for the JET-ILW based on near infrared imaging diagnostic systems. The outline of the present article is as follows. In section 2 we discuss the choice of central wavelengths and widths of the interference filters as well as the advantages and disadvantages of a first wall protection system based on NIR cameras. The section also covers the analysis of the impact of the plasma continuum radiation on the measurements in different wavelength ranges. Additionally, we discuss in section 2 the spectral emissivity of the main JET-ILW materials and its dependence on measurement wavelength, temperature of the surface and surface roughness. The impact of these parameters on the accuracy of surface temperature measurements is examined. Section 3 introduces the near infrared imaging system on JET-ILW including the cameras and optical components. In addition, the in-vessel calibration of the imaging diagnostics is described in the following section. A short description of the software framework for data analysis of imaging system is given in section 5. In section 6, an example for the activation of the real-time protection system is presented and its reliability is discussed in section 7. Section 8 reports surface temperature measurements under harsh conditions in the presence of dust on the surface as well as of deposited layers. Finally, a summary and conclusions are given in section 9.

2. Wavelength selection

2.1 Selection of the wavelength range

Non-contact optical temperature measurements are based on the detection and the analysis of thermal radiations emitted by an object. The physical effect used for such thermographic measurements is the variation of number of photons emitted per surface unit at the wavelength, λ , with the temperature of the blackbody, T , as it is given by Planck's law [6]. The detector signal, S_{det} , in fusion devices is a composition of signals due to the thermal emission of the target, S_{therm} , of continuum plasma emission (mostly bremsstrahlung), S_{brems} , and of fluxes reflected from the sample surface, S_{refl} :

$$S_{det} = K(\lambda) \left(\frac{\epsilon \frac{c_1 L}{\lambda^5}}{\left(\exp\left(\frac{c_2}{\lambda T}\right) - 1 \right)} + S_{brems} + S_{refl} \right) \quad (1)$$

Here K is a calibration factor for a given detector system at given λ , ε is the emissivity of the target, $c_{1L}=2hc^2$ and $c_2=hc/k=14388\mu\text{m K}$ are the first and the second radiation constants, k is the Boltzmann constant, h the Planck constant, and c the speed of light.

The maximum relative error of the temperature measurement can be calculated from Eq.(1):

$$\frac{\Delta T}{T} = \frac{\lambda T}{c_2} \left(\frac{e^{c_2/\lambda T} - 1}{e^{c_2/\lambda T}} \right) \left[\frac{\Delta K}{K} + \frac{\Delta \varepsilon}{\varepsilon} + \frac{(S_{brems} + S_{ref}) \times \Delta K / K + \Delta S_{det} / K}{\varepsilon L(\lambda, T)} \right] \quad (2)$$

Here $L(\lambda, T) = \frac{c_{1L}}{\lambda^5} \frac{1}{(\exp(\frac{c_2}{\lambda T}) - 1)}$ is a spectral radiance emitted by a blackbody at temperature T and at wavelength λ .

The maximum relative error estimation is performed in a way similar to that presented by A. Herrmann et al. in [7]. In addition to the method described in [7], the signal contributions due to bremsstrahlung, reflected light and error due to the non-ideal detector have been

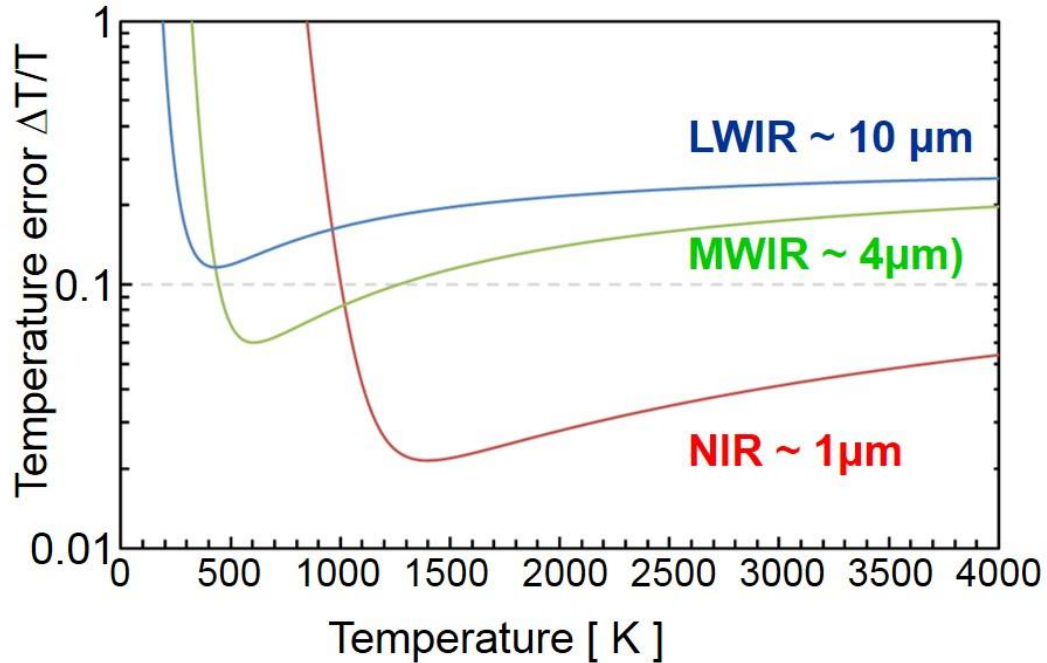


Fig.2 The maximum relative error for NIR, MWIR and LWIR detection system for the temperature measurements on the tungsten surface.

considered. The measurement error becomes greater with the wavelength and with the target temperature. However, at small temperatures close to the detection limit, the bremsstrahlung contribution becomes significant and it increases the measurement error significantly.

Figure 2 shows the maximum relative error as a function of the temperature of a tungsten surface for three different wavelengths. Based on experiments, the following assumptions were made for the estimation of the error:

$$\text{NIR: } \varepsilon = 0.42; S_{ref}/\varepsilon L(\lambda, T) \approx 0.05; \frac{\Delta K}{K} \approx 0.05; \frac{\Delta \varepsilon}{\varepsilon} \approx 0.10$$

$$\text{MWIR: } \varepsilon \approx 0.15; S_{ref}/\varepsilon L(\lambda, T) \approx 0.1; \frac{\Delta K}{K} \approx 0.05; \frac{\Delta \varepsilon}{\varepsilon} \approx 0.15$$

$$\text{LWIR: } \varepsilon \approx 0.10; S_{ref}/\varepsilon L(\lambda, T) \approx 0.1; \frac{\Delta K}{K} \approx 0.05; \frac{\Delta \varepsilon}{\varepsilon} \approx 0.10$$

As will be discussed in section 2.4, the emissivity of the W target at the wavelength of $\approx 1\mu\text{m}$ changes only slightly with surface temperature. For MWIR and LWIR measurements, however, the emissivity varies strongly with surface temperature: for example, in case of detection using MWIR ($\lambda=4\mu\text{m}$) from 0.08 at $T=1000\text{K}$ to 0.14 at 2000K . Such a strong variation of the emissivity with surface temperature leads to larger relative errors for the calibration factor and emissivity in the case of MWIR and LWIR. Moreover, the contribution of the reflected light to the error is larger for longer wavelengths, owing to a smaller emissivity and, correspondingly, to a proportionally larger reflection from the W surface.

Measurements in the NIR are thus more robust against changes of parameters like the emissivity, in particular for tungsten surfaces. The relative error for the temperature measurements with a NIR detector is below 2% in the relevant temperature range from 700°C ($\approx 973\text{K}$) to 1730°C ($\approx 2000\text{K}$), which is fulfilling the requested measurement accuracy of $\pm 50^\circ\text{C}$. In contrast to NIR detection, the temperature error for the measurements with MWIR and LWIR sensors is much larger and amounts to about 7-20%; it cannot fulfil the requested measurement accuracy of $\pm 50^\circ\text{C}$. Based on this analysis, the shortest possible wavelength has been chosen for the infrared protection system.

2.2 Feasibility of NIR Emission Measurements

Reliable measurements of the surface temperature are only possible when the background emission intensity is low. The measurements of the thermal emission of the target could be contaminated with plasma bremsstrahlung emission, and emission due to free-bound transitions (recombination). To demonstrate the feasibility of NIR thermal measurements, estimates of background intensities are discussed in this section.

Figure 3 shows the relative contributions of the continuum free-free, free-bound and thermal spectral radiance given a 2 m thick homogenous deuterium plasma without impurity seeding. The effective plasma ion charge, Z_{eff} , experimentally observed on JET-ILW in unseeded plasmas is below 2.0. During monitoring pulses without impurity seeding in JET-ILW an average $Z_{\text{eff}}=1.21$ is observed [8]. For the estimation of the lowest detectable surface temperatures, we consider the most critical case with strong bremsstrahlung level assuming $Z_{\text{eff}} = 2.0$.

The bremsstrahlung intensity as well as free-bound hydrogenic intensity was calculated using ADAS [9]. Plasma parameters for these estimates were chosen to determine typical high and low levels of Bremsstrahlung $P_{brem} \sim n_e^2 Z_{eff} T_e^{-1/2}$ [10]. The high density (10^{20}m^{-3}), low electron temperature case ($T_e = 5 \text{ eV}$), represents the detached plasma conditions and low density ($2 \times 10^{19} \text{m}^{-3}$) and high electron temperature ($T_e = 50 \text{ eV}$) are typical parameters for the attached divertor on JET-ILW.

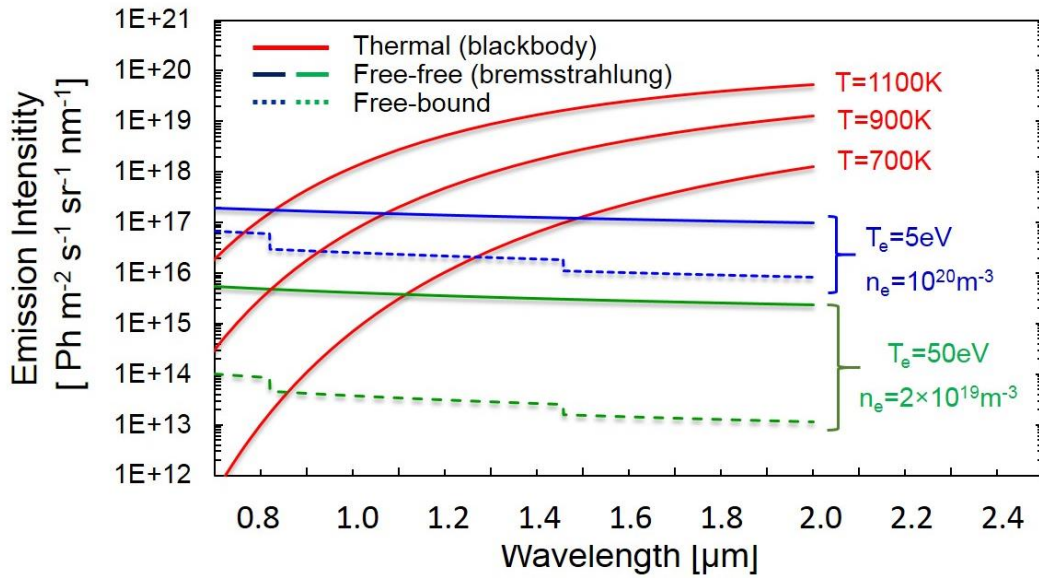


Fig.3 Calculated continuum emission spectrum contributions from Bremsstrahlung, radiative recombination and thermal emission for a 2 m thick isotropic deuterium plasma without impurity seeding. Here an effective charge of $Z_{eff} = 2.0$ is assumed.

The thermal emission was calculated using Planck's blackbody emissivity formula for three surface temperatures, 700K, 900K and 1100K. The free-bound emission intensity is low and can generally be neglected. The bremsstrahlung emission starts competing with thermal emission only at very high densities, high Z_{eff} levels and surface temperatures below 1000K. For temperatures in excess of 1000K the thermal emission will dominate in the NIR spectral range. The lower limit for temperature measurement with NIR systems is thus around 1000K, fulfilling the requirement for protection systems at JET-ILW.

2.3 Selection of the interference filters for the NIR Cameras.

The near infrared imaging system for the real-time protection provides an advantage for the optical design because widely used conventional optics and image sensors can be used. In addition, optical material and component properties are much more tolerant to radiation and plasma effects in the NIR range. To select interference filters with optimized full-width at half

maximum (FWHM), an initial survey of the plasma emission spectrum in the NIR spectral range has been performed in the JET-ILW torus with the help of the mirror-linked divertor spectroscopy system [11]. In the survey, a commercial 0.5 m Czerny–Turner spectrometer equipped with a CCD detector was used.

Fig.4 shows a survey spectrum from the JET-ILW divertor. The survey was composed of two spectra taken in two reproducible, auxiliary heated JET-ILW discharges. Few emission lines can be seen in the wavelength range from 960 and 1060 nm. The line emission-free regions are candidates for NIR thermal measurements. Based on analysis of the NIR spectra, two types of

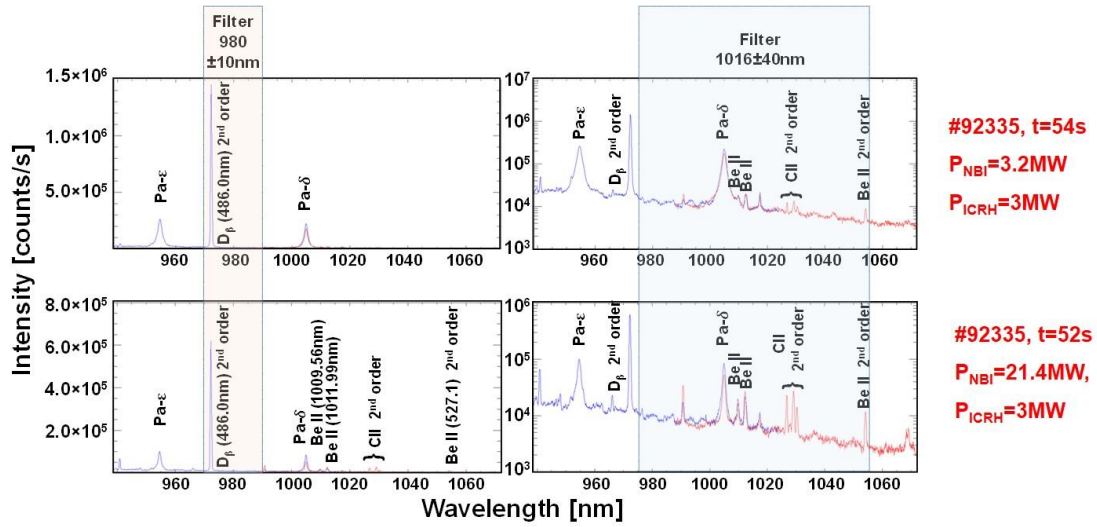


Fig4. Spectra measured in the divertor region.

band pass filters have been used: 980 ± 10 nm and 1016 ± 40 nm. The spectral range of the filter $\lambda 980 \pm 10$ nm is completely free of spectral lines. The one seen at 972 nm is a second order of the D_β spectral line (486 nm) which has no impact on the measurements of thermal radiation.

The spectral coverage of the NIR filter with central wavelength at 1016 ± 40 nm contains the Paschen spectral line (Pa- δ) of deuterium (transition 7-3) at 1000.46 nm. Because the probability of ionising the highly excited atom (in this case to the level $n=7$) is very high, the deuterium atoms will be quickly ionised before emitting a photon. Correspondingly, the intensity of this emission line of recycled deuterium under attached divertor conditions is below our detection limit for the surface temperature observations and can be neglected. However, this emission line must be taken into the account in the case of strongly recombining plasmas. In this case, the population of the high levels is dominated by recombination and is much larger than the population through excitation. Thus, the emission Pa- δ is strongly coupled to the plasma continuum radiation. Nevertheless, the integral over the continuum radiation inside the filter

window is a factor of 2 larger than the Pa- δ line intensity. The Pa- δ emission has an impact on the thermal measurements only in the case of strongly recombining plasmas when the measurements are not possible anyway due to the strong continuum radiation.

2.4 Spectral emissivity of JET-ILW materials

The emissivity of the surface of a material is its effectiveness in emitting energy as thermal radiation. Each material has a different emissivity. Emissivity is a dimensionless quantity which can range from a theoretical value of 0.0 (completely not-emitting) to the value of 1.00 (completely emitting). The surface/object is called blackbody if the emissivity of the material equals to 1. However, it is important to point out that, generally, emissivity is not constant as it depends on several parameters such as wavelength, temperature of the surface and its roughness.

The JET-ILW main chamber is protected by limiters made of castellated beryllium tiles. The divertor consists of CFC tiles coated with a 12-20 μm tungsten layer and one horizontal tile composed of bulk tungsten lamellas. For surface temperature measurements with high accuracy, as required for the JET-ILW wall protection, the knowledge of the spectral emissivity of each material in use is essential.

The tungsten spectral emissivity, shown in Fig. 5a for different surface temperatures, is well documented [12]. The so-called “X-point of W”, where the emissivity wavelength isotherms cross, corresponds to $\lambda \approx 1.27 \mu\text{m}$. The usage of the cameras equipped with interference filters (IFs) at the central wavelengths of 980nm and 1016nm, close to the “X-point,” brings the advantage of a weak dependence of ϵ_λ on temperature. The emissivity of the W coatings deposited on CFC (Dunlop DMS 780) was investigated in the range of 700 –1200°C [13]. A value of 0.63 ± 0.07 at $\lambda = 1064 \text{ nm}$ was found for 10 μm thickness, while for 20 μm the spectral emissivity was 0.59 ± 0.06 . This spread of values is due to the structure of the CFC substrate. In the temperature range 700–1200°C, there is no significant dependence of the W coating emissivity on the surface temperature at $\lambda = 1.064 \mu\text{m}$. At higher wavelengths (1.75 μm and 4 μm), though, the emissivity increases with temperature. No significant change of the

emissivity after plasma exposure in JET-ILW (experimental campaigns in 2011-2012) was detected for the vertical W-coated CFC Tiles 3, 4 and 7 [13].

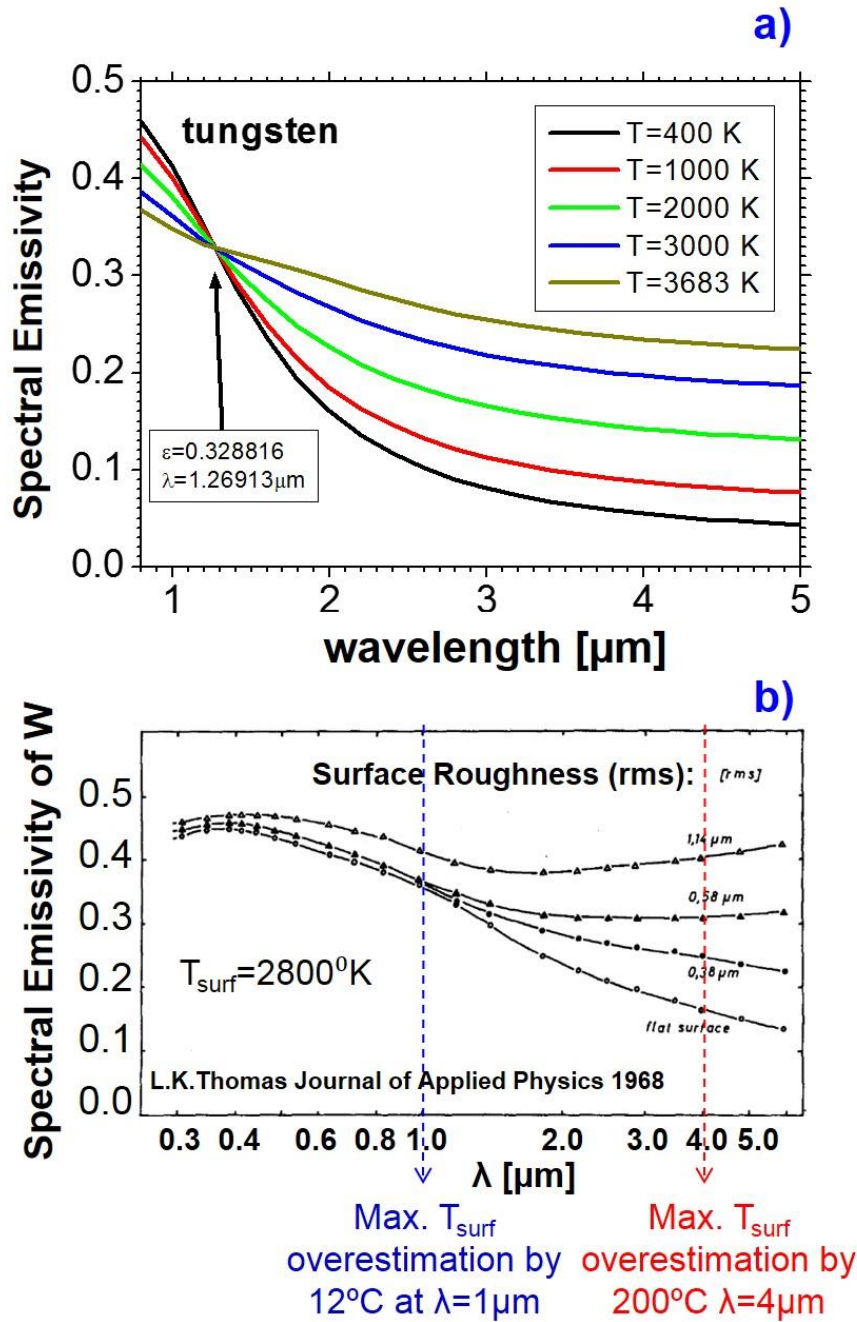


Fig. 5. a) W spectral emissivity according to [12] and b) the normal spectral emissivity of W with different surface roughness in dependence of wavelength [14].

Additionally, beryllium emissivity measurements have been performed on a neutral beam test bed. The values of emissivity used for the protection NIR imaging cameras (with 1016 ± 40 nm) are: bulk tungsten $\epsilon=0.42-1.98 \times 10^{-5} \times T$ (K); W coatings $\epsilon=0.6$; beryllium $\epsilon=0.25$.

The surface roughness could have a significant impact on the emissivity of the object [14]. As shown in Fig5b [14] the surface roughness (rms) of about 1 μm could lead to the increase of

spectral emissivity by the value of $\Delta\varepsilon \approx 0.02 - 0.05$ at $\lambda=1\mu\text{m}$. In the MWIR wavelength range the impact of the surface roughness on the spectral emissivity is even stronger: for example the surface roughness of $0.38\mu\text{m}$ ($1\mu\text{m}$) leads to increase in the emissivity from 0.16 to 0.24 (0.4) at $\lambda=4\mu\text{m}$ and at surface temperature of 2527°C (2800°K). For NIR measurements of surface temperatures around 1000°C , such a roughness provokes a relatively small emissivity uncertainty of $\frac{\Delta\varepsilon}{\varepsilon} \sim 0.05 - 0.125$ leading to a maximal temperature overestimation by 16°C . In contrast to NIR measurements, the MWIR and LWIR detection is much more strongly impacted by the surface roughness due to the smaller emissivity values at longer wavelengths: the emissivity inaccuracies are $\frac{\Delta\varepsilon}{\varepsilon} \sim 0.50 - 1.0$ for the MWIR method for the expecting surface roughness $0.38\text{-}1.0\mu\text{m}$. Such larger uncertainties on the emissivity could lead to the significant overestimation of the surface temperature. For example, the MWIR method with accuracy of $\frac{\Delta\varepsilon}{\varepsilon} \sim 0.50$ will overestimate T_{surf} by 200°C for measurements in the temperature range around 1000°C , thus exceeding the accuracy measurement requirements ($\pm 50^\circ\text{C}$) of the real-time

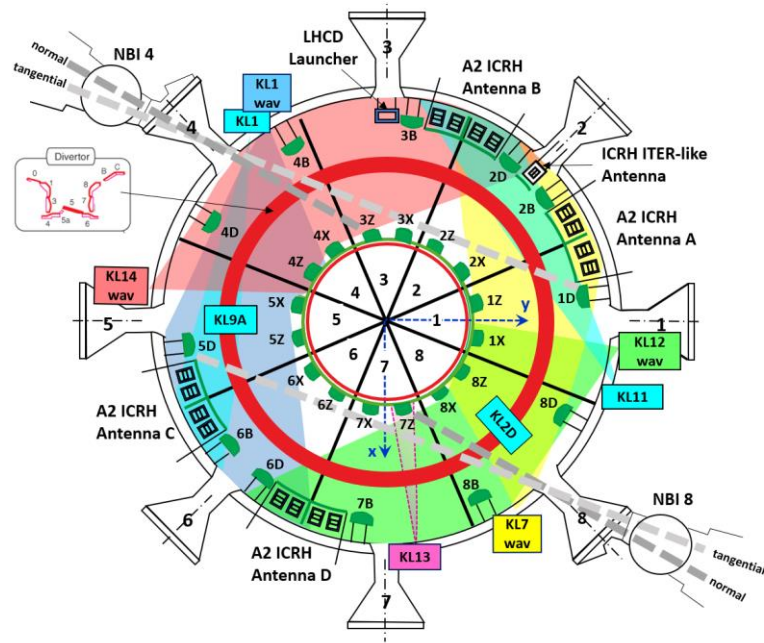


Fig.6 Top view of the JET tokamak. Fields of View (FoV) of protection NIR CCD cameras. KL1 div, KL11 div and KL2D have 2 cameras for each view.

protection system.

Recent measurements of the roughness of the bulk W material of tungsten lamellae which had not been exposed to the plasma show an even larger surface roughness $2.1\text{-}2.6\mu\text{m}$ [15] supporting the choice of NIR for the first wall protection system. The roughness of the Be tiles

installed on the machine is below $3\mu\text{m}$ [15] and roughness measurements of the W coated CFC tiles are planned for this year [15]. Due to the strong dependence of the emissivity on the surface roughness, the values of the emissivity measured on original JET-ILW W coated CFC tiles [13] are used for the calculation of the surface temperature from the NIR measurements. Further studies of the impact of the surface roughness on the spectral emissivity are required.

From the analysis of the response of the surface temperature on the heat loads we can conclude that some of the wall components coated with thin layers demonstrate a classical heat up and cool down behaviour: a slow increase of the temperature by applying heat loads as well as a slow temperature reduction after removal of the heat load source. This is an indication of the good thermal contact of the layer to the underlying material. The layer could be composed of different materials with unique spectral emissivity, which could dynamically change during the experimental campaign. The deviation of the emissivity by $\Delta\epsilon/\epsilon=\pm 0.5$ from the nominal value of the bulk material could be expected which will lead to the reduction of the accuracy of the NIR method to ($\pm 50^\circ\text{C}$). The surface temperature measurements of such mixed material is very complicated and requires a multi-spectral approach. In JET, a novel self-calibrated method which is based on the operation of two or more cameras at different wavelengths in the NIR and MWIR spectral range is under development. It does not require the absolute calibration of individual camera systems. Demonstration and test of this method are foreseen in 2019; they are out of the scope of this paper.

2.5 Advantages and Disadvantages of the Machine Protection System based on NIR Cameras

This section summarizes the advantages and disadvantages of a machine protection system based on NIR cameras:

The advantages of the NIR Infrared Thermography measurements are:

- possible usage of widely-used conventional optics and image sensors
- silicon based image sensors can be used.
- moderate prices of the silicon based cameras due to a wide choice of suppliers.
- optical material and component properties are much more tolerant to radiation and plasma effects in the NIR range
- the lower limit for temperature measurement with NIR systems is at about 700°C ($\approx 973\text{K}$). Hence they can fulfil the requirement for protection systems at JET-ILW.

- the error for the temperature measurements with an NIR detector is relatively small (up to 2%) for the relevant temperature range from 700°C ($\approx 973\text{K}$) to 1730°C ($\approx 2000\text{K}$).
- the robustness of the protection system based on the NIR recording method against changes of system parameters such as the emissivity.

The disadvantages of the NIR Infrared Thermography measurements are:

- The bremsstrahlung emission starts competing with the thermal emission at very high densities and high Z_{eff} levels at surface temperatures below $\approx 973\text{K}$. Thus, measurements below 700°C ($\approx 973\text{K}$) are not possible. This lower detection limit is below the protection limit.

3. The Near Infrared Imaging System on JET-ILW

3.1 Protection Cameras

For reliable operation of the imaging system in the hostile electromagnetic environment of JET-ILW, the protection cameras must meet the following main criteria of an undisturbed operation of CCD sensors and electronics in the presence of a magnetic field and acceptable resistance to neutrons and gamma radiation. Video cameras should operate without replacement at least one year, withstanding a neutron fluence of $\sim 2 \times 10^{12} \text{ n/cm}^2$ [16]. In contrast to a digital video camera, an analogue one can fulfil these criteria easily because of its robustness and stable operation

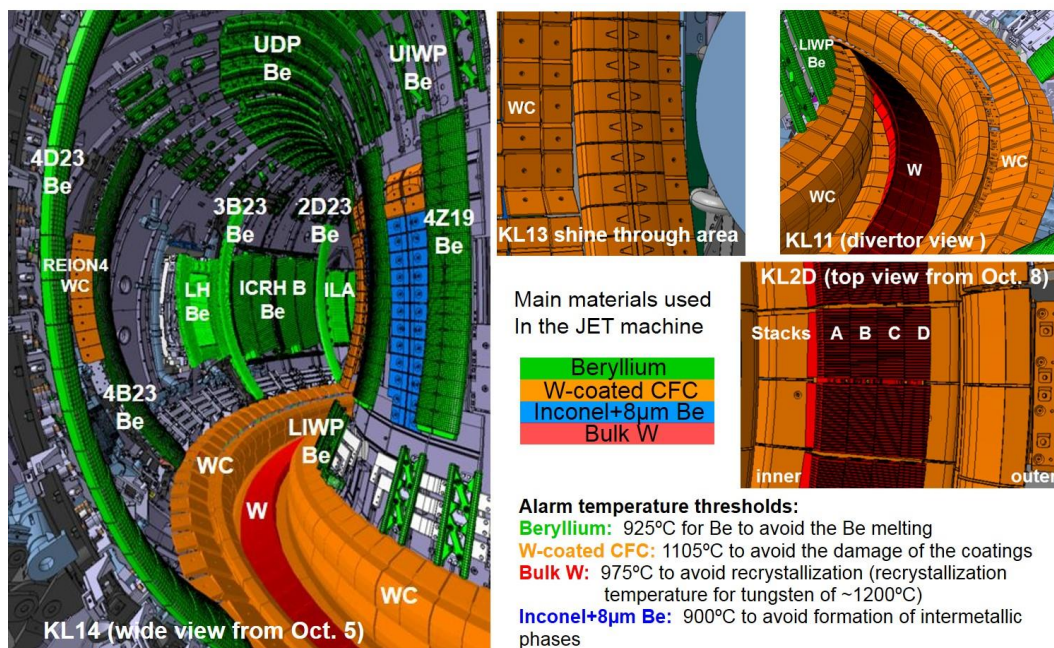


Fig.7 Fields of View (FoV) of protection NIR CCD cameras.

under harsh electromagnetic as well as radiation conditions – features which are particularly desirable in protection systems. Digital cameras contain significantly more electronics (analogue and digital) than analogue cameras. The electronics responsible for the digital signal processing make these cameras more fragile under harsh conditions. Given the same environmental conditions, analogue cameras suffer only from the impact on the imaging sensor, whereas digital cameras show a strong response to hard radiation and neutrons due to failure of the camera digital electronics [16]. The drawback of analogue cameras is the rather low sensitivity around 1 μm wavelength (<10%) for silicon-based detectors and the low dynamic range of the uncooled CCD sensor (8bit) [17]. Indeed, digital cameras produce video signals by digitizing the signal at, or using an ADC placed close to, the CCD array, rather than at a separate frame grabber. This enables relatively high spatial resolution (larger images), high intensity resolution or high dynamic range (bit depth), high speed and low noise level. The JET-ILW imaging system for machine protection is based on analogue monochrome CCD cameras (Hitachi KP-M1AP; sensor: Sony ICX423AL, Sensor size 768x576, pixel size: 11.6 μm (H) \times 11.2 μm (V) [18]), equipped with near infrared (NIR) filters. Synchronized with the external sync signals (V/H scans), the cameras operate in non-interlaced mode at 50 fields per second with binning (odd and even lines are exposed together at the same time). In this mode, the spatial resolution is lost in the vertical direction: the camera delivers images with an apparent size of 720×288 pixels every 20ms. At the same time, the pixels are effectively larger in the vertical direction, and hence more sensitive.

The cameras are mostly located at the equatorial plane as well as at the top of the machine and are distributed across the different octants. Fig.6 shows the locations of the protection NIR CCD cameras on JET-ILW. Imaging systems use four wide angle views, four tangential divertor views, two top views of the divertor, and one view of the NBI shine through area covering 66% of the main chamber wall and up to 43% of the divertor.

Figure 7 shows examples of the fields of view of different imaging systems on JET-ILW. Different colours represent the different materials of the first wall: green – beryllium; red – bulk tungsten; orange – W-coated CFC; blue – Inconel coated with 8 μm Be. The most important components for which the temperature should be routinely monitored are the beryllium inner and outer limiter, bulk tungsten in the divertor and the W-coated horizontal and vertical divertor CFC tiles. Different camera systems have different spatial resolutions: ≤ 3 mm for divertor view cameras (KL11 and KL1), ≈ 2 mm cameras with divertor views from the top of the machine (KL2D) as well as with a view of the shine-through area (KL13), ≈ 10 mm for cameras with wide angle view (KL14 and KL12). This needs to be taken into account when using the system,

because the delivered temperatures are values averaged over the area defined by the spatial resolution of the specific camera. It is found [19,20] that the inter-ELM upstream power fall-off length λ_q^{mdp} (mm) in the JET-ILW for attached divertor conditions can be described by the empirical scaling [19,20]:

$$\lambda_q^{mdp} = 0.73 B_T^{-0.8} q_{cyl}^{1.2} P_{SOL}^{0.1} R^{0.0}$$

where B_T (T) describes the toroidal magnetic field, q_{cyl} the cylindrical safety factor, P_{SOL} (MW) the power crossing the separatrix and R (m) the major radius of the device. The analysis of λ_q^{mdp} at the outer midplane was performed for a wide range of H-mode pulses indicating a variation between 1mm and 4mm. At the divertor target, the power fall-off length could be an order of magnitude larger (as shown in [19] and [20]) due to the magnetic field geometry, making it possible to resolve the heat loads with divertor view cameras even at $\lambda_q^{mdp} = 1mm$.

The typical alarm temperature thresholds used for the real-time protection of the first wall on JET-ILW are:

- Beryllium: 925°C for Be to avoid melting
- W-coated CFC: 1105°C to avoid damage of the coating
- Bulk W: 975°C to avoid recrystallization (recrystallization temperature for tungsten of ~1200°C)
- Inconel+8µm Be: 900°C to avoid formation of intermetallic phases [21].

The time resolution of 20ms is not enough to resolve the surface temperature excursion during the Edge Localised Modes (ELMs). As shown in [19], the ELM duration τ_{ELM} in JET-ILW varies strongly between 0.1 and 4ms depending on the plasma conditions and the average ELM duration is about 2ms which is much shorter than the time resolution of the cameras. Thus, the measured surface temperature corresponds to a value averaged over 20ms, which could include both inter and intra-ELM phases (if ELM frequency is above 50Hz). Even if the alarm temperature threshold used for the real-time protection of the first wall made of Bulk W is 1000°C to avoid recrystallization (recrystallization temperature for tungsten of $T_{recrys} \sim 1200^\circ\text{C}$), the maximum researchable surface temperature during the large ELMs could exceed T_{recrys} . As reported in [22], the resultant surface temperature increase during the ELM was about $\Delta T = 250\text{--}300^\circ\text{C}$ in the experiments with 3MA/2.9T high energy confinement mode (H-mode) pulses with an input power of $P_{in} = 23$ MW, a stored energy of 6 MJ as well as regular type I ELMs at ELM energy loss of $\Delta W_{ELM} = 0.3$ MJ and at a frequency of 30 Hz. It should be mentioned here that this experiment was designed to provide ELM-induced melting of a specially misaligned W lamella in the divertor. Operating at temperatures close to the protection limit (1000°C) could

lead to the peak ELM temperatures beyond T_{recrys} for a short time period on the time scale of the ELM duration. Note that recrystallization is a thermally activated process in which the material crystal structure is modified due to the nucleation and growth of new, strain-free grains (grain growth), reducing the internal residual stress of the material. The process is associated with a reduction in material strength/hardness, shock resistance and an increase in ductility and is a function of time at given temperature and temperature gradients [5,23]. The time duration of the ELMs (of about $t_{\text{ELM}}=1\text{ms}$) is short and is considered not to be sufficient to support the recrystallization process. Additionally, a typical grain length is around $100\text{ }\mu\text{m}$ and the width is about $20\text{-}40\text{ }\mu\text{m}$ for ITER tungsten components. Heat loads with 1ms pulse duration will heat up a surface layer of thickness of about $50\text{-}100\mu\text{m}$ which is of the same order as the grain sizes. For an effective recrystallization process, the heatable volume has to exceed at least 100 times the volume of a single grain. The post-mortem analysis of the bulk W as well as of the CFC coated tungsten layer, exposure after campaign in 2011-12 (ILW-1) and after the following campaigns in 2013-14 (ILW-2) do not show any signature of W recrystallization [15]. The transient heat loads applied by laser irradiation [24] (pulse duration of 1ms , heat power loads between $0.1\text{-}0.9\text{GW/m}^2$) on ITER-grade tungsten also confirm this statement.

No melting of bulk tungsten occurred for typical large ELMs at JET-ILW with $\Delta W_{\text{ELM}} = 0.3\text{ MJ}$. Such ELM heat load values correspond to a heat flux factor value ($F_{\text{HF}} = P \times t_{\text{ELM}}^{0.5}$, where $P = 100\text{MW/m}^2$, taking into account an equal ELM energy sharing to inner and outer divertor targets) [25] of about $3\text{MJ m}^{-2} \text{s}^{-1/2}$ which determines the surface temperature rise caused by the transient heat load event. This heat flux factor is much less than the melting heat flux factor for W (tungsten melting occurs for $F_{\text{HF}} > 40\text{-}50\text{ MJ m}^{-2} \text{s}^{-1/2}$) and corresponds to a surface temperature increase during the ELM of about $\Delta T = 250^\circ\text{C}$ which is in line with experimental observations [22]. Such a temperature increase is too low to lead to a melting of the tungsten components (the melting temperature of W is $T_{\text{melt}}^{\text{W}} = 3695\text{K}$ (3422°C))

To test the feasibility of the protection system to avoid tungsten melting, the protection system was activated during the dedicated experiment on JET-ILW designed to investigate the consequences of transient W edge melting on ITER [22]. For the purpose of these experiments a specific tile (with misaligned lamellae) of the horizontal, outer divertor target was modified in order to introduce a leading edge and thereby expose a W surface in JET-ILW to transient power densities relevant to the standard divertor surface in ITER during an unmitigated transient. The surface temperature of the misaligned lamellae was controlled by the protection system. In this test, the pulse was terminated and the peak temperatures during the ELMs remained below 1600°C demonstrating the effectiveness and reliability of the protection system.

3.2 Examples of the divertor view and wide angle viewing system at JET-ILW

The majority of the imaging systems are mirror-based and are installed inside the JET-ILW vacuum vessel. Figures 8 and 9 show examples of the divertor view and wide angle viewing system at JET-ILW.

A new endoscope [26, 27] with an improved spatial resolution and thus delivering images of high quality, gives a unique opportunity for monitoring the surface temperature of the divertor tiles in the NIR spectral range. The endoscope covers the spectral range from 390 nm to 2500nm with a high optical transmittance ($\geq 60\%$ in the NIR wavelength range) as well as a high spatial resolution, that is less than 2 mm at the object plane. The spatial frequency at 50% of the modulation transfer function (MTF) in the image plane is larger than $15 \lambda/\text{mm}$. The endoscope field of view (FOV) covers an angle of $\pm 8^\circ$ and the object distance is 4m. In addition to scientific cameras in the near UV and VIS wavelength range, the imaging system includes two protection cameras in the near infrared range which take advantage of the same FOV. The endoscope contains hardware for *in situ* relative measurements of the endoscope transmission and is

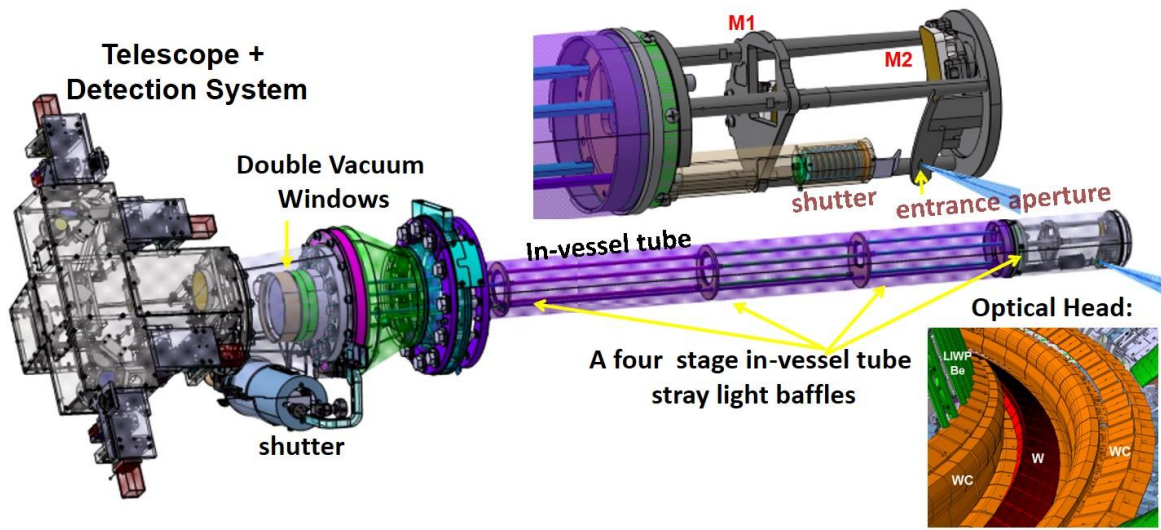


Fig.8: Mirror-based endoscope (KL11) for divertor spectroscopy on JET.

reasonably well protected against coating of the first optics by impurities from the plasma. This has been achieved with a physical entrance pupil of diameter ≤ 8 mm. The system should be able to operate in a strong magnetic field: up to $B=3.0$ T toroidal magnetic field at the optical head, where the poloidal and radial field can change at 70 and 20 T/s respectively. Additionally, the system is designed to withstand without damage or loss of alignment accelerations up to 7 g that can result from disruptions.

The design concept is based on reflective optics, mainly to be able to sustain high neutron radiation but also to avoid chromatic aberrations. The optical system consists of two main components: the endoscope optical head and the external telescope assembly. The optical head with entrance aperture and front mirror unit is located in-vessel, i.e. in the vacuum, whereas the external telescope optical assembly is located outside the vessel.

The mirrors in the endoscope head are off-axis and made of Al 6061 with an optical surface manufactured by single point diamond turning. The surface was left uncoated to mitigate a possible risk of degradation of the mirror coating in the in-vessel environment. The external telescope images the FOV, via the intermediate image generated by the endoscope head optics, onto the focal planes of the various camera systems. The external telescope consists of a four-mirror aspherical off-axis arrangement and a beam splitter unit, the first optical element of which is the reflective 50/50 beam splitter (BS). Detailed information about this mirror based endoscope system as well as about the detection system can be found in [26, 27].

Figure 9 shows an example of an ITER-like wide-angle system (KL14 camera system) on JET-

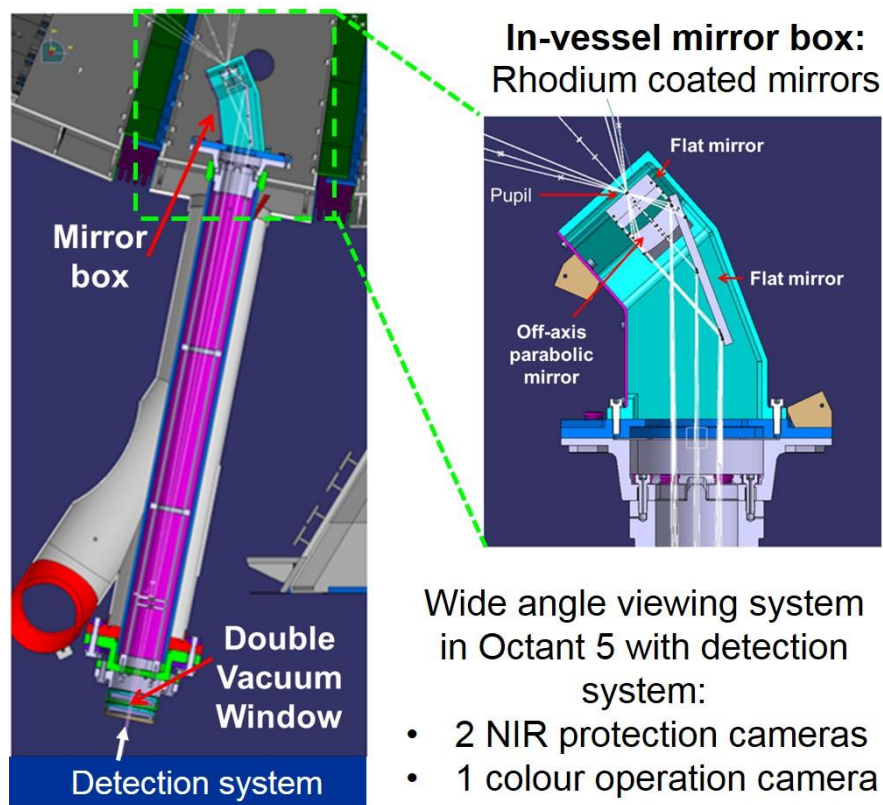


Fig. 9 A wide-angle view imaging diagnostic (KL14) with all reflective, in-vessel optics on JET-ILW.

ILW. The wide angle camera system has been installed in JET-ILW in 2014. It is composed of an in-vessel mirror box with 3 stainless steel mirrors coated with rhodium (Rh) which view the torus through a conically shaped aperture. The mirror setup delivers the required image quality

for plasma monitoring and wall protection. Rhodium is an important candidate material for first mirrors, especially in ITER [28, 29]. Rhodium provides a better reflectivity (70-80%) in the visible spectral range [30] as well as near-infrared and infrared ranges (around 85% at 1 μ m). Rh has also a low chemical reactivity, preventing oxide and carbide formation [31, 32]. As mentioned above, this system, composed of a mirror box with 3 stainless steel mirrors coated with Rh, is attached to the vacuum vessel wall on the low field side of the JET-ILW torus. The mirror system contains two branches, a lower and an upper branch. Each of the branches views half of the machine through a conically shaped pupil with a minor diameter of 3 mm. A 30° off-axis parabolic mirror with a focal length of 50.8 mm creates an intermediate image of the object inside the box close to the surface of the next, flat mirror. The half images of the two branches are then combined on the camera sensor to form a full wide-angle view image. The detailed description of the wide angle imaging system is given in [33, 34].

The stability of the optical transmittance of the protection system is an important issue and is monitored during each JET-ILW shutdown phase with the help of an in-vessel integrated sphere as will be shown in section 4. Additionally, systems like KL11, shown in figure 8, include options for the in-situ calibration of the endoscope transmittance during the experimental campaign, which allow the continuous tracking of possible degradation with time. The measured transmittance of the entire endoscope system for wavelengths $\lambda > 500$ nm does not show any detectable altering of the transmittance [26,27]. For $\lambda < 500$ nm we observe some degradation ($\approx 40\%$ at 400 nm). It is assumed that the degradation is caused by impurity deposition on the first mirror. The operation of the protection cameras in the NIR wavelength range is thus not affected by any transmittance change at wavelengths around 1 μ m. Also the absolute calibration of the scientific cameras coupled to the KL11 system do not show any changes since 2012, confirming the long term transmittance stability of the mirror based system above $\lambda=500$ nm.

The wide-angle imaging system KL14 discussed above (figure 9) contains two CCD cameras, colour and monochrome, each of it equipped with a telephoto zoom lens set to a focal length of 250 mm and 300mm respectively. An unfiltered colour CCD camera provides video images for general plasma operation monitoring in the visible spectral range. The composite RGB signal of the unfiltered colour CCD camera is routinely split into three colour channels: Red: 580-750nm; Green: 475-570nm; Blue: 430-480nm. The colour channels have been compared using monitoring pulses, a procedure which is regularly performed during the JET-ILW operation and analysed on possible brightness changes due to transmittance altering. No or an insignificant degradation of the optical transmittance has been observed [34].

More information about the imaging systems used on JET-ILW for the real-time protection of the first wall can be found in [26,27,33,34,35].

4. In-vessel Calibration of the Imaging Diagnostics for the Real-Time Protection

The calibration of the imaging systems has been performed with help of integrating spheres coupled to a stable, broad spectrum light source of known radiance. The in-vessel calibration

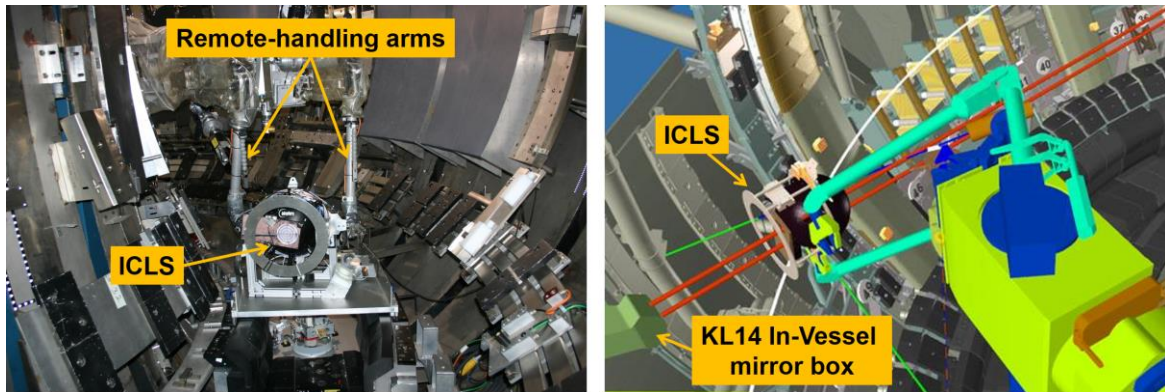


Fig.10 In-vessel Calibration of JET-ILW Protection Cameras with help of ICLS.

light source (ICLS) [36] with a 4 inch diameter exit port and four halogen lamps was positioned by the remote-handling arm inside the JET-ILW vacuum vessel (see Fig.10). The spectral radiance L_λ of the ICLS lamps is maximal in the NIR wavelength range and is thus best suited for the calibration of protection cameras. The ICLS contains two internally mounted 100 W Tungsten-Halogen bulbs (lamp1 and lamp 3) providing a spectral radiance of $\sim 0.92 \text{ W m}^{-2} \text{ sr}^{-1} \text{ nm}^{-1}$ at $1 \mu\text{m}$, which corresponds to a brightness temperature of $T_{\text{br}}=975^\circ\text{C}$ and $T_{\text{br}}=958^\circ\text{C}$ at $0.98 \mu\text{m}$ and $1.016 \mu\text{m}$ correspondingly. The brightness temperature, T_{br} , is defined as the temperature of a blackbody that emits an identical amount of radiation at the same wavelength as measured from tungsten-halogen bulbs.

Additionally, two 5 W Tungsten-Halogen bulbs have been internally installed in the integrated sphere providing a spectral radiance of $\sim 0.035 \text{ W m}^{-2} \text{ sr}^{-1} \text{ nm}^{-1}$ at $1 \mu\text{m}$ (which corresponds to the brightness temperature $T_{\text{br}}=703^\circ\text{C}$ and $T_{\text{br}}=660^\circ\text{C}$ at $0.98 \mu\text{m}$ and $1.016 \mu\text{m}$ correspondingly). Furthermore, the integrated sphere under different operation modes (different lamps or different combination of the lamps) has been cross-calibrated against a Pegasus R blackbody with the emissivity of $\epsilon = 0.995$ controlled by a thermocouple with an uncertainty of $\pm 2^\circ\text{C}$. The temperature uncertainty found by using the direct calculation of the T_{br} from spectral radiance and by using the comparison with black body is below 5%. Acquired brightness temperatures have been used for in-situ calibration of all protection cameras. As a result of the

in situ calibration, the operational temperature ranges for the materials used on JET-ILW are: Be 700-1400°C; W coating 700-1370°C; W 700-1400°C. The detailed description of the in-vessel calibration of the protection imaging system can be found in [37].

The operation time of the ICLS lamp should be reduced to a minimum to keep the ICLS lamp radiance unchanged over the calibration period during the shutdown phase. Therefore, special

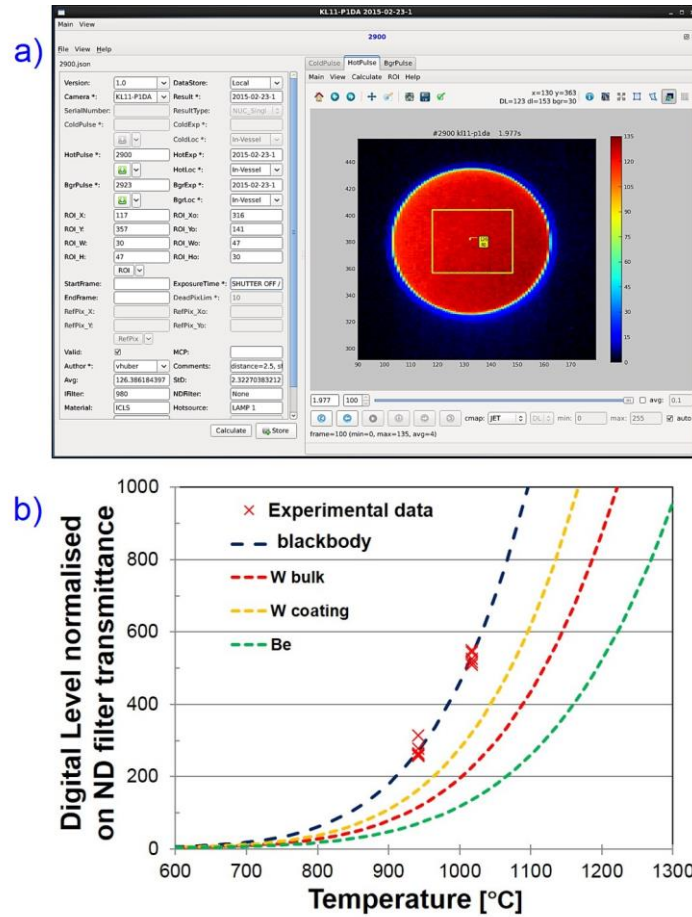


Fig. 11 a) Calibration software for data evaluation and b) digital levels measured by the camera versus brightness temperatures of the ICLS with one lamp and with a combination of two lamps.

software for the data acquisition and quick data analysis are required. A new powerful software package *calib* [37] has been developed and proved successful operation during the calibration of the protection cameras as well as of visual and MWIR imaging systems. It consists of several components based on the newly developed framework JUVIL (JET Users Video Imaging Library (see section 5), which provides easy access to the video data of different cameras installed at JET-ILW. The calibration software provides rapid data acquisition and analysis of measured data during the calibration experiments, stores the calibration settings for each

experiment to the central JET database and produces the calibration curves for beryllium, bulk W and W coatings taking into account the emissivity for each material surface.

To confirm the calibration of the protection cameras, the response of the protection system to main chamber and divertor hot spots was commissioned during the JET-ILW plasma restart. Validation of the temperature outputs from the camera's real time processing unit (RTPU, see below) was performed by cross comparison of the protection cameras against each other. Fig.12a shows the comparison of the surface temperature of the bulk tungsten measured by protection cameras during the plasma discharge, demonstrating a sufficiently good agreement

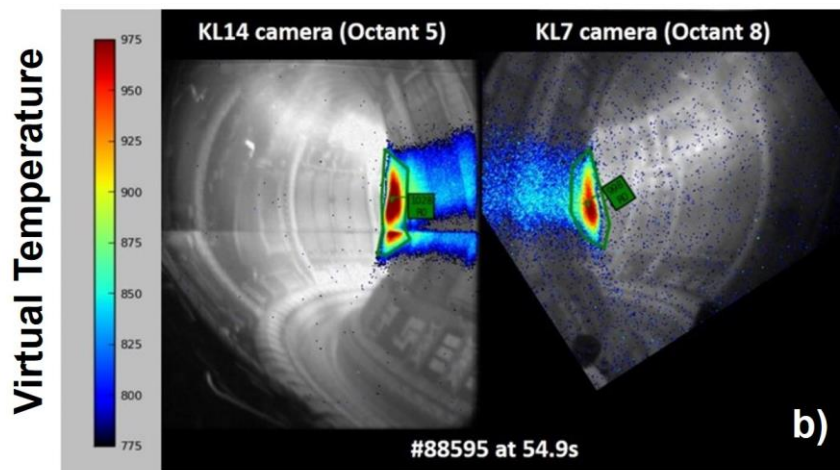
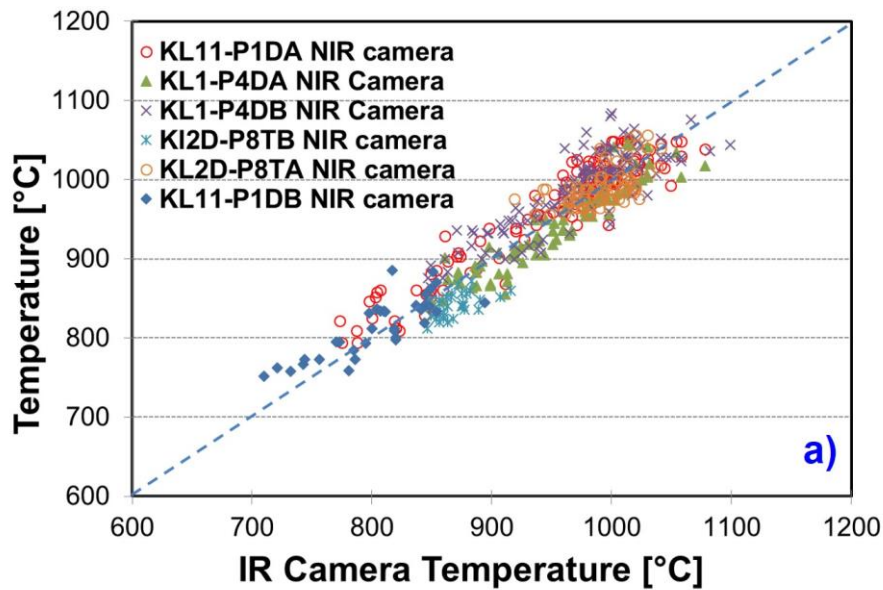


Fig.12 a) $T_{\text{surf}}^{\text{NIR}}$ versus $T_{\text{surf}}^{\text{IR}}$ (left) and b) temperature validation during inner wall MARFE phase.

between the NIR and IR spectral ranges.

Up to 800°C, the protection camera overestimates the temperature due to continuum radiation.

Note that the cameras contributing to Fig 12a are located in different toroidal locations, so the

discrepancies could be explained by deviations in the toroidal symmetry. Because of the small dynamic ranges of the protection cameras, we use several of them, configured to give measurements in different temperature windows. Additionally, the temperatures measured by protection cameras have been compared with the thermal IR camera (at the 4- μm wavelength) [38] as shown in Fig.12a. Above 800°C, the agreement between the protection cameras and the thermal IR camera is within 5% on average.

The validation of the wide-angle cameras in the main chamber has been performed during a discharge phase with an inner wall Multifaceted Asymmetric Radiation from the Edge (MARFE) [39]. We used the fact that the MARFE provides strong continuum radiation in the NIR range with an excellent toroidal symmetry. The “virtual” temperatures delivered by JET-ILW wide-angle cameras are consistent within 4%, confirming the reliability of the in-vessel calibration (see Fig.12b) [37]. The cross-validation NIR cameras observing the beryllium evaporator, equipped with a thermocouple, also demonstrate a good agreement within 20°C at $T_{\text{surf}}=900^\circ\text{C}$.

5. Software Framework for Data Analysis of JET-ILW Imaging Systems

A new powerful software framework JUVIL (JET Users Video Imaging Library) [40] has been developed and successfully installed at JET-ILW for fast data visualization and advanced analysis of all types of imaging data. The JUVIL framework is based on modular object-oriented components implemented in *Python* to simplify work with JET-ILW scientific data. It provides standard interfaces to access video data and post-processing, which are highly configurable and can be easily extended and adapted for new data formats and imaging cameras.

JUVIL contains a Logbook Editor and Logbook Viewer. The Logbook Editor loads automatically the raised VTM events as well as the alarms during an arbitrary pulse and stores them to the logbook. The Logbook Viewer is useful to display and to analyse the list of VTM events. Additionally, a specifically developed Hotspot Editor is recognized as an excellent tool for the investigation of the formation and development of hot spots and for their evaluation [40]. Detailed information about the Software Framework for Data Analysis of JET-ILW Imaging Systems is given in the appendix.

6. Real-Time Protection System in Action

The surface of the JET-ILW divertor is protected against melting by six video imaging cameras, (see field of views in Fig. 6). The divertor tiles are chamfered in the toroidal direction to avoid

leading edges (the so-called shadowing). Nevertheless, damages of the tungsten coatings or bulk tungsten tiles can happen in the high heating power plasma pulses.

Regions of interest (ROI) are chosen for the selected PFCs and used to configure a Real Time Processing Unit (RTPU) for each camera (see Fig.13). The description of the software for the production of ROIs is given in [40]. The RTPU analyses the camera data in real time, and the maximum temperature measured in each ROI is sent, for each 20ms data frame, to a separate real time system - the vessel thermal map (VTM). The VTM determines, with all available input on materials and locations, the likely cause of the overheating and requests an appropriate response from the plasma control system by sending an alarm to the Real Time Protection Sequencer (RTPS). The RTPS is a highly configurable system and controls the actuators and

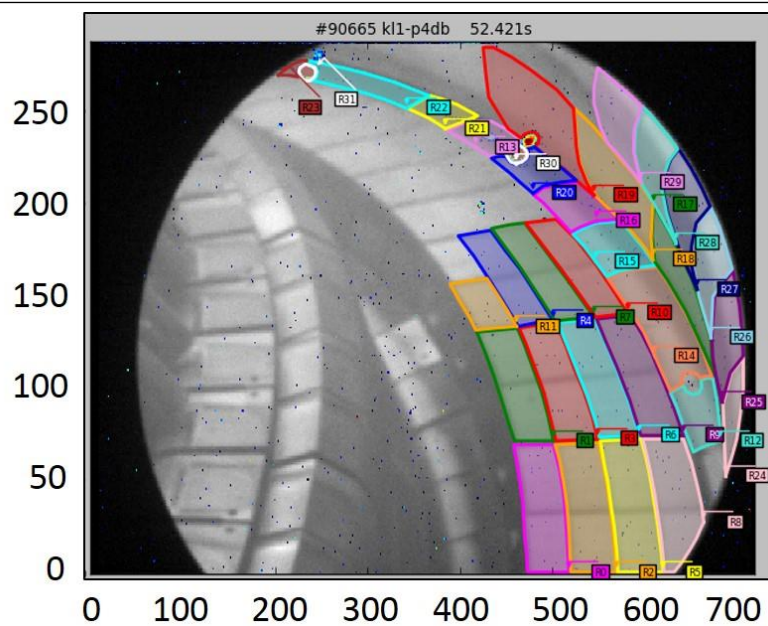


Fig.13 Regions of interest (ROI) for the selected PFCs.

safely terminates the plasma, thereby reducing the risk of a disruption or other potentially

damaging event. Detailed description of the video digitization and distribution, the real time processing system as well as real time processing algorithm can be found in the appendix.

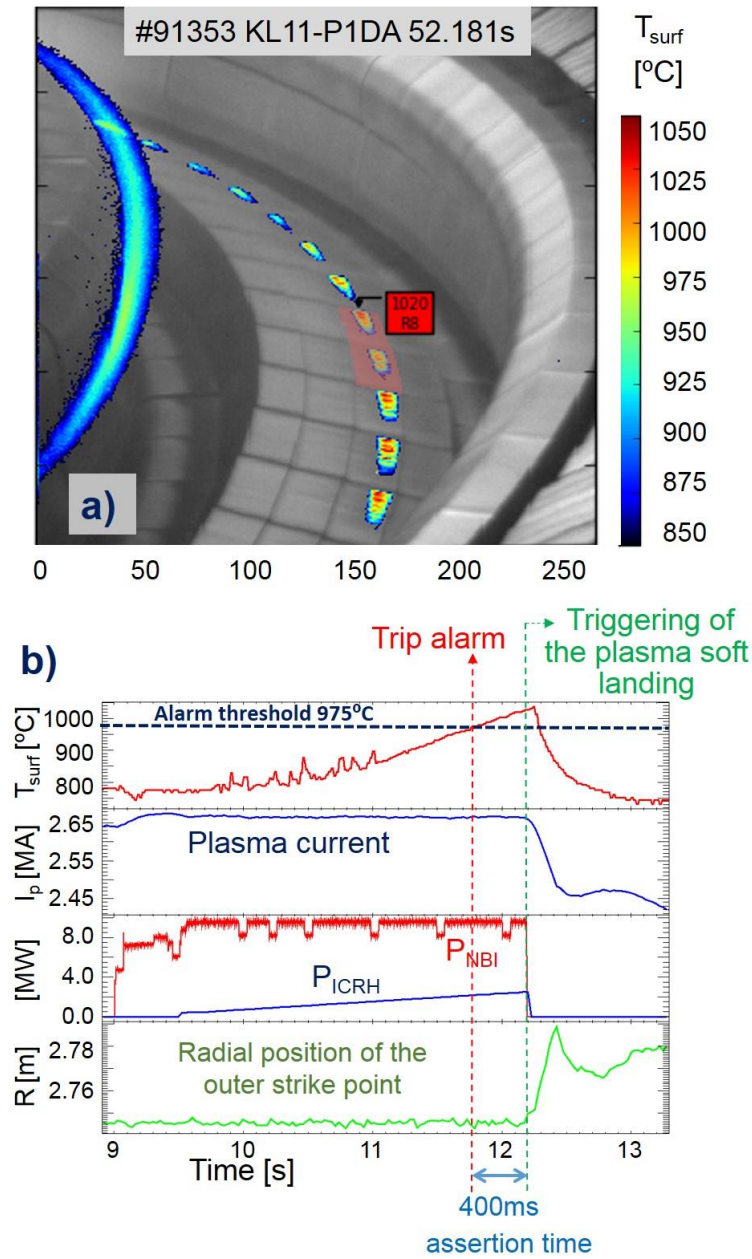


Fig.14 A discharge with a classical heat up of the divertor W bulk tiles.

Fig.14 shows a discharge demonstrating a typical heat-up of the divertor W tiles. The outer strike point, where the heat flux is maximal, is located on the bulk tungsten tile. This pulse was an ELMy high energy confinement mode (H-mode) plasma with auxiliary heating power of about 12MW ($P_{NBI}=9.6\text{MW}$ and $P_{ICRH}=1.0\text{-}2.5\text{MW}$). The surface temperature increases with time during the auxiliary heating phase. At 11.8s the surface temperature of the bulk tungsten tile reaches the trip level of 975°C and remains above this trip level for longer than the assertion time, which is 400 ms. At time 12.2s the VTM sends an alarm to RTPS requesting an

appropriate action from the plasma control systems. As a result the plasma is carefully terminated by switching off the auxiliary power, moving the strike points away and ramping down the plasma current. The “assertion time” is the time window during which VTM checks that the temperature of the analyzed surface is consistently above the trip level. This is needed to avoid false alarms due to spurious signals on the camera image (e.g. caused by neutron impact). During the response time of the plasma control systems after receiving the tripping level, the temperature still increases and reaches the maximal value of 1030°C, which is significantly below the threshold at which the bulk tungsten re-crystallizes (1200°C).

7. VTM Alarm statistics

For JET-ILW operations, minimizing the number of early plasma pulse terminations due to

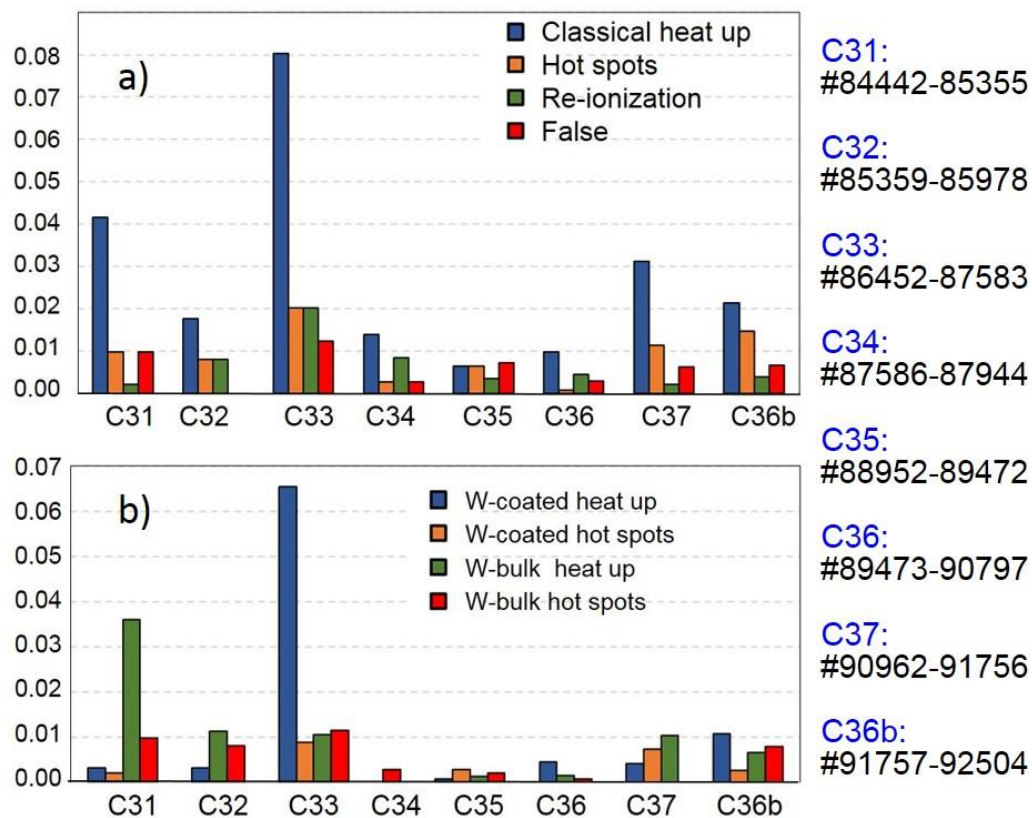


Fig. 15: a) Number of alarms per campaign normalized to number of the total campaign shots b) divertor alarm statistics.

VTM alarms itself is a key objective in order to prevent loss of experimental time and preserve the lifetime of the first wall components. An analysis of the reasons for the early termination of plasma pulses is therefore crucial for optimal machine operation. In order to provide a fast data visualization and advanced analysis of all types of VTM alarms, a new software, *VSO Logbook Editor* [40], has been developed and successfully installed at JET-ILW.

The features of the *VSO Logbook Editor* significantly reduce the time needed for the interpretation of an event by the VSO. After analysis, the VSO specifies the type and category of the VTM event from the predefined lists in the Event Editor and store the results in the VSO Logbook on the JET-ILW centralised file system.

All VTM alarms on the JET-ILW machine are thus well characterised and catalogued. An analysis of the reasons for early termination of plasma pulses is shown in Figure 15a. Here the number of alarms per campaign normalized to total number of campaign shots is displayed. Directly after implementation of the protection system on JET-ILW during the campaigns C31, C32 and C33, the statistics showed a large number of VTM alarms due to classical heat up of the first wall components, to hot spots formation and to heating of the NBI beam re-ionization zones. The latter correspond to the limiters subjected to the impact of the re-ionised neutrals injected by the heating system. The majority of alarms due to classical heat up of the wall components occurred during the H-mode plasmas with additional neutral beam as well as ICRH heating. After the discharge was terminated by RTPS, plasma operation was then modified (by reduction of the heating time window, increasing the gas fuelling, changing the magnetic plasma configuration, etc.) to avoid a further undesirable stopping of the next plasma discharges.

During the C33 campaign, about 8% of the plasma discharges were terminated by RTPS to avoid harmful situations like dangerous overheating through classical heat up of the wall components. Also the number of hot spots (2% of the plasma pulses) as well as the alarms due the NBI beam re-ionization (2%) increased. The following campaigns C34-C36 show a general tendency of reduction of the VTM alarms because of the continuous improvement of the real-time protection system as well as a better understanding of the physics of events leading to the alarms. Within the last experimental campaigns (C37 and C36b) a significant improvement of the auxiliary heating systems on JET-ILW has been performed leading to a marginal increase of the plasma terminations due to the RTPS safety system: about 2-3% are due to the classical heat up and about 1-1.5%, to the hot spot formation. As shown in figure 15, the false alarms were reduced to less than 0.5% of all plasma discharges, even though the total additional heating power increased significantly in these campaigns.

The VSO Logbook Viewer can also display the list of VTM events on the specific segments and physical tiles as shown in Figure 15b. It presents an analysis of the VTM alarms caused by overheating events in the divertor region. It can be seen that, because of the protection of the divertor against overheating, about 3% of the plasma discharges were terminated by RTPS.

During the C33 campaign, about 6.5% of the plasma discharges were terminated by 74 alarms: 71 on horizontal divertor target Tile 6 and 3 alarms on the vertical outer divertor target Tile 7.

8. Difficulties of the surface temperature measurements in the case of dust on the surface and deposited layers

Protection of the bulk tungsten and tungsten coated CFC tiles in the divertor as well as Be wall components in the main chamber is more of a challenge due to signal artefacts produced by

- neutrons,
- dust on the surface
- deposited layers and
- delamination of the W coated CFC divertor tiles

that often generate false hot spots. A hot spot validation algorithm was successfully integrated into the real-time system and is now used to avoid alarms caused by neutrons and dust. The detailed description of the Real time processing algorithm is given in appendix.

Dealing with the deposited layers is more complicated because their size prevents the protection system to detect the surface temperature from a clean surface and the surface layer will cause a wrong estimation of the temperature. The option to modify the strike point position avoiding the surface layers altogether is not always possible as this might have an impact on the divertor pumping and plasma performance. The dilemma can be overcome by periodic sweeping of the divertor strike point positions, which will be discussed below in section 8.3. Deposited layers rise when eroded material, possibly from a different tile, deposits on a surface. On the tungsten coated CFC such layers typically reach a fraction of a mm thickness and can vary from soft to hard and potentially break up, generating transient impurity events and jagged edges.

Such deposits can either increase the emissivity (so as to give too high temperature reading) or decrease (temperature underestimated). They also tend to have a poor thermal contact with the substrate and therefore heat up more rapidly and to higher temperatures than clean surface. In addition, the jagged edges of damaged layers can receive higher heat fluxes than the original, carefully shaped surface.

Despite of the all metal first wall in JET-ILW these layers might still be carbon (from existing deposits on the wall), beryllium or redeposited tungsten on beryllium and tungsten. The detailed discussion about material migration and the formation of deposited layers in the JET-ILW divertor region can be found in [41,42,43].

In this section we will discuss three cases of hot spot formation on the limiter surface with deposited layers, on the partly delaminated divertor tiles and on the horizontal divertor tiles with thick deposited layers.

8.1 Hot spot formation on the poloidal limiter during the limiter plasmas

Figure 16 shows an example of an ohmic discharge during which a hot spot on the inner beryllium limiter has been observed. The hot spot is located at the upper part of the inner wall guard limiter (fig.16a,b), which is typically 7cm away from the separatrix.

Assuming 10° for the incidence angle of the field lines with respect to the plasma-facing surface and an ohmic heating power of 1MW, the power density on a surface perpendicular to the magnetic field is about 0.05MW/m^2 for a power decay length in the SOL of 0.03m. The temperature rise on beryllium in 10s should thus be below 100°C which is an overestimation as the power crossing the SOL is assumed to flow only one way along field lines rather than to both direction to inner and outer divertor targets.

However, the surface temperature measured by the protection system shows a fast initial rise (from 800°C to 900°C in 0.2s (fig.16c)) which suggests that the measurement is not the result of thermal radiation from the bulk. Such a temporal response of the temperature (quick

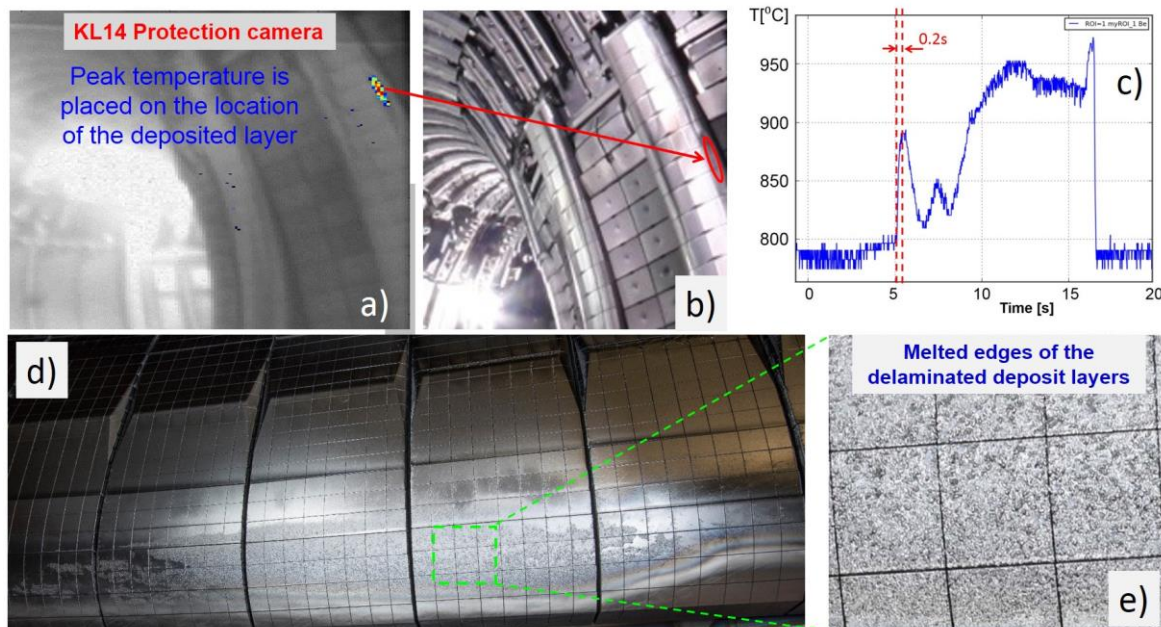


Fig. 16 a,b) Hot spot on the inner wall guard limiter c) a temporal response of the temperature at the location of the hot spots d) thick deposited layer at the location of the monitored hot spots on the Be limiter e) melted edges of the delaminated deposited layers.

temperature increase and decrease) is typical signature for a deposited layer with poor thermal contact with the material substrate.

Assuming that the incident power is absorbed in the deposited layer (the thermal capacity of which can be neglected) and that the heat loss of the layer is only through radiation, we estimate the temperature of the thin deposited layer rises to about 900-1000°C, which is consistent with the measurements of the protection cameras. Here it is assumed that the emissivity of the deposited layer is $\varepsilon=0.25$. However, the layer could have a larger emissivity for layer thicknesses larger than 0.5µm.

In-vessel inspection of the JET-ILW first wall with a high resolution camera during the last shutdown, shown in figure 16d, demonstrates clearly the existence of a deposited layer on the limiter. The VTM alarm event was accordingly caused by a partially delaminated deposited layer. Figure 16d shows this thick deposited layer at the location of the monitored hot spots on the Be limiter. Due to its high thickness, the deposited layer starts delaminate producing the jagged edges. The jagged edges of damaged layers receive higher heat fluxes provoking the local melting of the delaminated layer shown in the figure 16e.

In this case the hot spot should be ignored to avoid unwanted alarms. To ignore a given ROI, the user of the ROI Editor sets a flag to indicate that this ROI is “not under VTM control”, and this program’s output is used to change the VTM configuration to ignore these harmless overtemperatures. Another way to avoid the alarm that was used in JET-ILW limiter plasmas is to change the vertical position of the plasma, preventing the hot spot formation altogether.

8.2 Hot spot on the partly delaminated divertor tiles

Delamination of tungsten coatings on a few CFC based tiles was observed after the campaigns in 2013-2014 (ILW-2) [44]. This is associated with tiles which did not fully undergo the prescribed heat treatment at the time of production. Figure 17 shows the delamination on the lower outer vertical target. Significant heat loads in this region have resulted in a pattern of film cracking and delamination along CFC fibre planes in a toroidal orientation along the tile (fig17c). The delaminated areas give rise for concerns that they could be a source of carbon in the plasma. The eroded carbon can significantly impact the spectral emissivity due to its presence in the deposited layers. Ion beam analysis (IBA) data, however, including micro-beam Proton Induced X-ray Emission (PIXE) mapping, shows that Be and other heavy elements (W and Mo) are present on the delaminated surfaces of the low-field side outer horizontal target. In addition, scanning electron microscope (SEM) micrographs of cross sections show no evidence of erosion from the CFC surface or that thin deposits would have formed in delaminated regions. As is mentioned in [44] there is a known mechanism for failure of the coatings by carbidisation if surface temperatures exceed 1350°C for more than two hours [45]. However, this mechanism

has not been identified in the samples analysed so far because the protection limit is below this temperature. Crucially, the results of this analysis do show that in spite of the delamination of the W coating, the exposed surfaces are covered either by residual coating or deposits and therefore do not contribute to the carbon source in the machine. Figure 17a shows the hot spot formation on the lower outer vertical target during the ELMy H-mode plasma discharge with the additional input power of $P_{IN} = P_{NBI} + P_{ICRH} = 15\text{MW} + 3.5\text{MW} = 18.5\text{ MW}$. The experiments

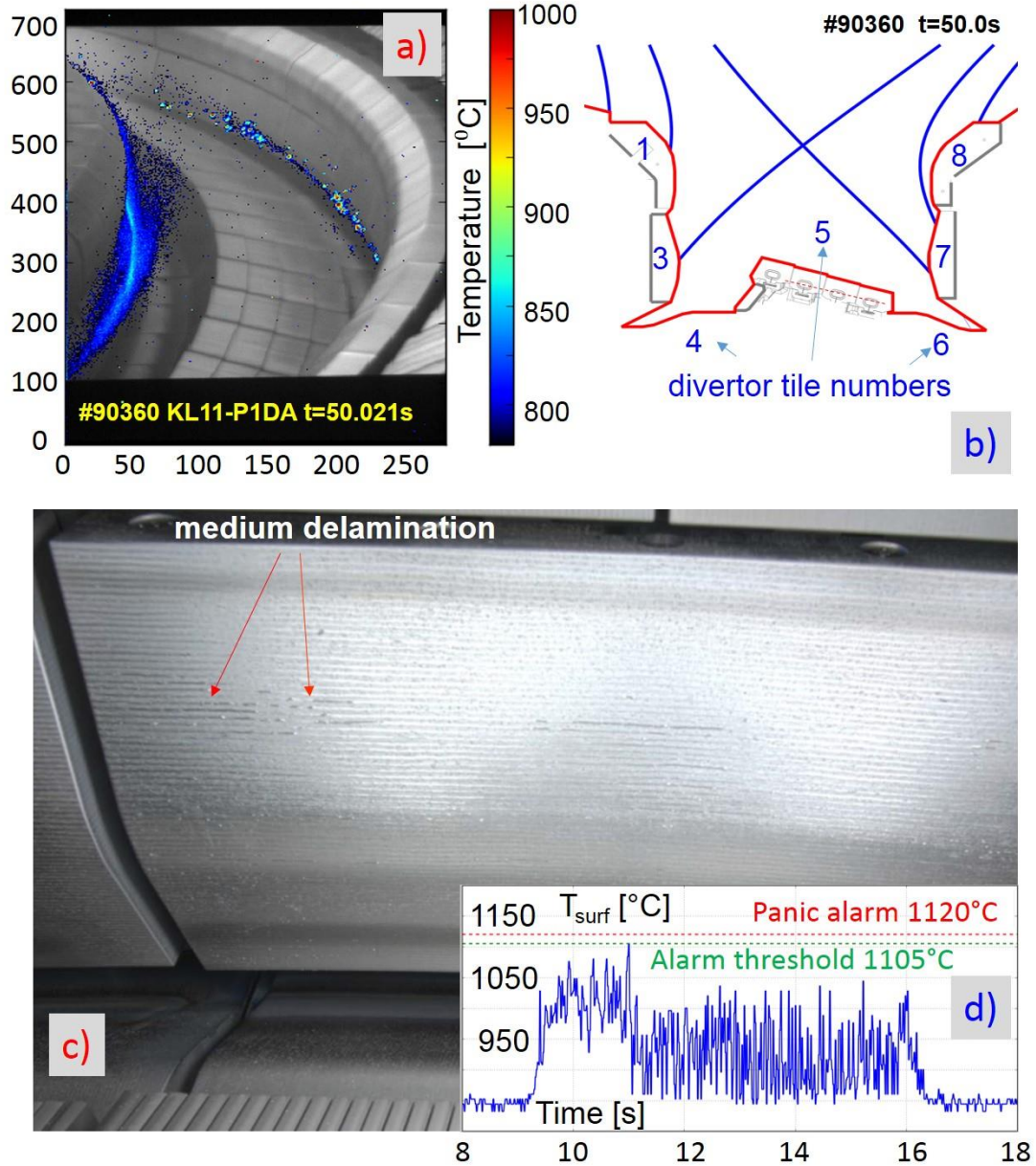


Fig. 17 a) Hot spot formation on the lower outer vertical target (tile7) during the ELMy H-mode plasma discharge b) magnetic equilibria with the strike points located on the vertical targets c) delamination on the lower outer vertical target (Tile7) d) time evolution of the measured surface temperature of the W-coated outer divertor target.

with the ILW have been performed at $B_T \approx 2.6\text{ T}$, $I_p = 2.5\text{ MA}$, in low-triangularity magnetic equilibria with the strike points located on the vertical targets. The temperature of the hot spots

rises quickly during the ELM up and cools down abruptly when the ELM is over (Fig.17d). This is a typical behaviour of overheated edges of delaminated layers. In the case shown, the ELM frequency is about 15Hz. At such a frequency the hot spots are seen on every third image frame. The temperature of the hotspots remains below the trip level (here 1105°C) during the entire pulse and therefore does not trigger the VTM alarm. Even if the temperature of the hot spots would have exceeded the trip level, at such ELM frequencies the time duration when the surface temperature is above the trip level (in this case 20ms) is shorter than the assertion time, and hence transient temperature rise would have not triggered an alarm of the protection system. As mentioned in section 3.1, the protection NIR cameras operate in non-interlaced mode at 50 fields per second. ELMs with frequency below 25Hz will lead to transient hot spot formation during alternate frame images and, correspondingly, will be ignored by the protection system. The strength of ELMs can be deduced from the loss in stored plasma energy. With an increase of the ELM frequency the loss in stored plasma energy during the ELM, the ELM energy loss, decreases because the ELM size E_{ELM} is inversely proportional to the ELM frequency f_{ELM} [46] ($E_{ELM} \sim 1/f_{ELM}$). For JET-ILW plasmas with an available auxiliary heating power of about 28MW and the heating power duration according the JET-ILW requirements, the ELMs with frequency beyond 25Hz do not lead to an increase of the temperature of the jagged edges to values above the tripping level. Thus the JET-ILW operation is in general not restricted due to delamination of the W-coating on the divertor tiles. The question is whether the protection system needs to be modified to protect the machine when the full power (34 MW of Neutral Beam Injection (NBI) and 6 MW of ICRH power) is applied. One possible solution is to increase the frame rate of the protection cameras. Suitable commercial silicon-based NIR cameras for the protection with a frame rate of 100frames/s are available on the market today.

8.3 Hot spot on the coated divertor tiles with deposited layers

Recent experiments with the ITER-like wall have demonstrated that changes in the position of the divertor strike point are correlated with a strong modification of the global energy confinement. The impact on energy confinement is observable both on the pedestal confinement and on normalised gradients of core density and temperature profiles. The plasma equilibria with strike points in the corner of the divertor show an increased core density gradient length

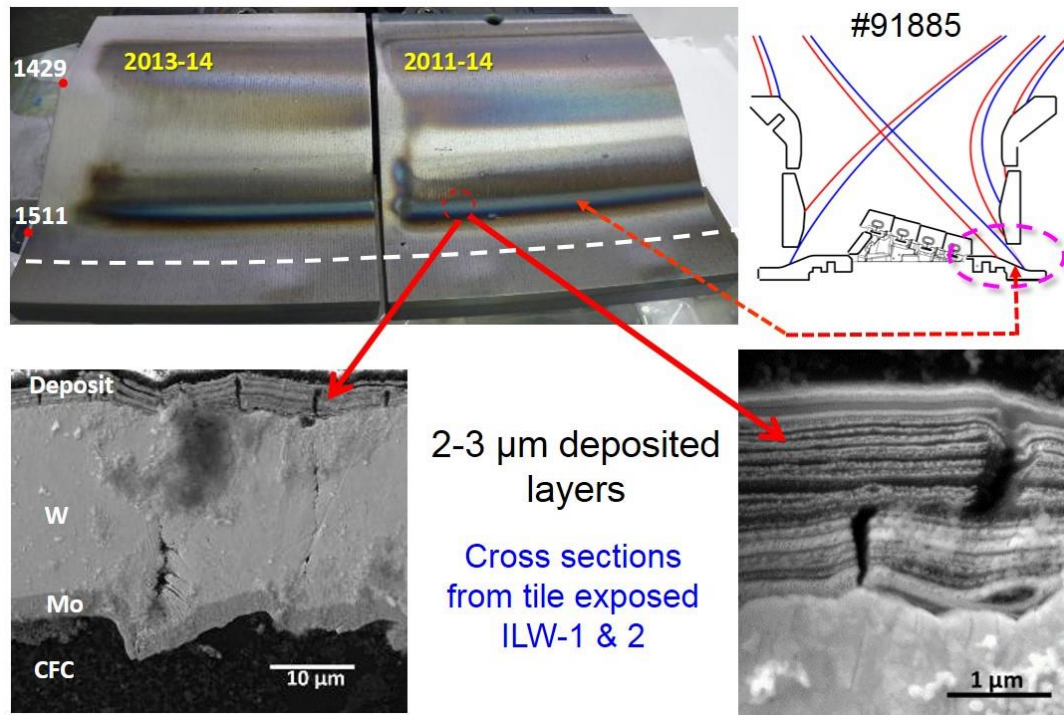


Fig. 18 Layered structure of deposit on the divertor horizontal Tile 6: 2-3 μm layered deposit. The dashed line shows the outermost location on tile 6 that can be seen by divertor view cameras, which is larger than the outermost location of the possible outer strike point location.

and ion pressure indicating a better ion confinement [47]. Thus, such plasma shapes are the preferred magnetic configuration for the JET-ILW experiments.

In the corner configuration the outer strike point is located on the horizontal target close to entrance to the pump duct. As reported in [48], this is a region of significant deposition, where a band of beryllium (Be) deposits has formed at the bottom of the sloping part of this tile (see Figure 18). Although visible after first campaigns with ITER-like walls in 2011-2012, the deposit was much thicker after the following campaigns in 2013-2014. Post mortem analysis of the surface of tiles removed from the JET-ILW vessel using ion beam analysis (IBA)

techniques such as nuclear reaction analysis (NRA) and elastic back scattering of protons (EBS) has revealed Be concentrations in the deposit $\sim 3.8 \times 10^{19}$ atoms cm^{-2} [49, 50, 51]. The deposit is layered as shown in Figure 18. The thickness of the deposited layers is about 2-3 μm .

The thermal contact of the layer with the substrate bulk could change with time, making the

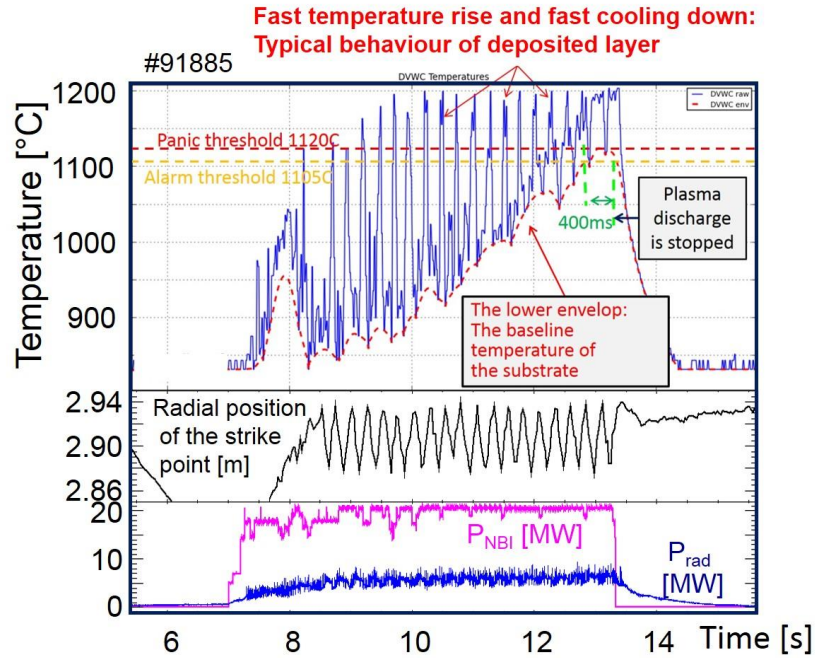


Fig. 19 Stopping the pulse during the protection of the horizontal divertor target with strike point on the deposited layer: top) the measured surface temperature of the W-coated outer divertor target; bottom) time evolution of a typical H-mode discharge with periodic strike point sweeping.

measured surface unpredictable. In other words, the operation in the static corner configuration will lead to overheating of the deposited layers, which will trigger the VTM alarm with consequent soft plasma stopping.

To avoid false alarms caused by overheating of deposited layers, periodic sweeping of divertor strike point positions has been proposed for experiments which have the outer strike point on the horizontal target. There are two benefits: firstly, the sweeping increases the area over which the heat is deposited, which is a known heat flux mitigation strategy. Secondly, provided the radial sweeping amplitude is larger than the poloidal dimension of the deposited layer patterns, the triggering of a false alarm due to layer overheating is avoided.

Figure 19 shows an example of a high power JET-ILW pulse with additional heating power of $\sim 20\text{MW}$. Magnetic field configurations for outer strike point location on the clean W-coated surface (red curve) and on the surface with deposited layer (blue curve) are shown in figure 18. The sweeping amplitude was 6cm and the frequency, f_{sweeping} , 4Hz. The measured surface temperature of the ROI covering the W-coated outer divertor target shows strong oscillations

with the maximal surface temperature coinciding with times when the outer strike point is located on the deposited layer and minimum values when the strike point is on the clean W-coated surface. An envelope of the measured surface temperature represents the temperature of the clean W-coated surface and, correspondingly, of the bulk substrate which is consistent with the MWIR measurements on the freshly installed Tile 6 in another toroidal location. At time 12.5s, the temperature of the bulk substrate (lower envelope) reaches the trip level of 1105°C and remains beyond this level longer than the assertion time (here $\tau_{\text{assertion}}=400$ ms). At time 12.9s an alarm is sent by the VTM and the plasma is successfully terminated. The example shown in figure 19 demonstrated that the video imaging protection system can work properly under these harsh conditions in the presence of deposited layers. To avoid the triggering of the VTM alarm the strike point should be swept between the surface with deposits and the clean W-coated surface during the assertion time of 400ms. In this case the surface temperature will not remain above the trip level during the assertion time and the VTM will ignore the spikes in the measured temperature caused by the deposited layers. This requirement provides the constraint for the lowest sweeping frequency: $f_{\text{sweeping}} > 1/(2 \times \tau_{\text{assertion}})$. In the case shown in Figure 19, the sweeping frequency f_{sweeping} should be larger than 1.25Hz. On the other hand, the sweeping frequency should not be too high due to the limited time resolution of the camera systems. This imposes an upper limit for f_{sweeping} of 25Hz to allow the NIR cameras to resolve the surface temperature oscillations.

9. Summary and conclusions

The ITER-like Wall protection system based on near-infrared video imaging was developed on JET-ILW and is operating reliably. Safe landing of the plasma is achieved when genuine hot spots are observed on the Be main chamber wall components as well as on the divertor PFCs (bulk tungsten and tungsten coated CFC tiles). Analog CCD cameras with the NIR interference filters are used to measure the surface temperature of the PFCs. The selection of interference filters for the NIR Cameras has been discussed. The NIR wavelength range is an optimal choice for monitoring of temperatures above 1000°C. The relative error for the temperature measurements with the NIR detector has been found to be relatively small (~2%) for the relevant surface temperature range from 700°C ($\approx 973\text{K}$) to 1730°C ($\approx 2000\text{K}$) fulfilling the requested measurement accuracy of $\pm 50^\circ\text{C}$. In addition, the usage of NIR provides the required robustness for the protection system, based on strategies against changes of system parameters such as emissivity. For NIR measurements of surface temperatures around 1000°C, a roughness about 1 μm provokes an uncertainty of the emissivity in the order of 0.05-0.125 leading to a maximal

temperature overestimate of 16°C. In contrast to NIR measurements, the MWIR and LWIR detection is very strongly affected by the surface roughness due to the smaller emissivity values at longer wavelengths. In plasma discharges with high densities and high Z_{eff} levels the bremsstrahlung emission makes measurements below 700°C ($\approx 973\text{K}$) impossible, defining the lower detection limit which is however below the protection limit. The sensitivity range of the protection system based on NIR diagnostic for the surface temperature is sufficiently large to cover the crucial temperatures at which material damage could occur.

The majority of the imaging systems are mirror-based and are installed inside the JET-ILW vacuum vessel. The assessment of the stability of the optical transmittance of the protection system during each JET-ILW shutdown phase has confirmed the long-term transmittance stability of the mirror based systems.

The imaging system has been calibrated in-situ with high accuracy using an radiometric light source, which has been brought inside the JET-ILW vacuum vessel by means of a remote-handling arm. As a result of the calibration, the detection temperature ranges for the materials used on JET-ILW are Be 700-1600°C, W coatings 700-1320°C, and W 700-1500°C. The validation of the wide-angle cameras in the main chamber has been performed during a discharge phase with an inner wall Multifaceted Asymmetric Radiation from the Edge (MARFE), confirming the reliability of the in-vessel calibration (see Fig.12b) [37]. The cross-validation NIR cameras with the beryllium evaporator, equipped with a thermocouple, also demonstrate a good agreement within 20°C at $T_{\text{surf}}=900^\circ\text{C}$.

A new powerful, software framework JUVIL (JET Users Video Imaging Library) has been developed and successfully applied at JET-ILW allowing fast post-pulse analysis of VTM events. This software contains a Logbook Editor which loads automatically the raised VTM events and alarms during a pulse and stores them to the logbook. A specifically developed Hotspot Editor is recognized as an excellent tool for the investigation of the formation and development of hot spots and for their evaluation.

A hot spot validation algorithm was successfully integrated into the real-time system and is now used to avoid alarms caused by false hot spots. It was demonstrated that video imaging protection system can work properly in the presence of neutrons, dust on the surface, deposited layers and delamination of the W coated CFC divertor tiles. Additionally, a method to avoid false alarms caused by an overheating of deposited layers has been discussed. A periodic sweeping of divertor strike point positions with optimized sweeping frequency as well as optimized assertion time has been proposed and successfully demonstrated in the experiments

in the so-called corner configuration. It has been shown that the pulse was safely terminated only once the temperature of the bulk substrate has reached the trip level.

The real-time video imaging system has been operated routinely over 12000 discharges since 2011. Within the last experimental campaigns about 2% to 3% of the plasma discharges were terminated by protection system to avoid harmful situations like dangerous overheating. The different detection algorithms fulfil their tasks reliably. False positive alarms have been reduced to less than 0.5% of all plasma discharges.

Acknowledgements

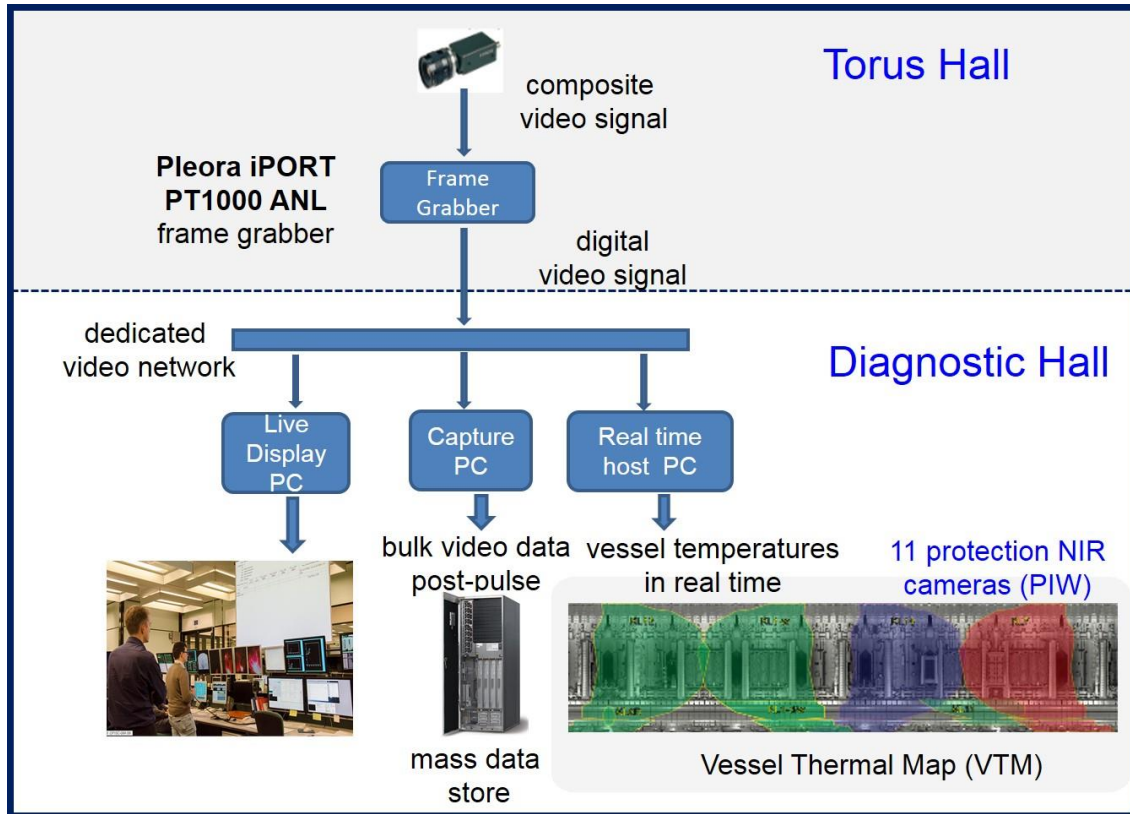
This work has been carried out within the framework of the EUROfusion Consortium and has received funding from the Euratom research and training programme 2014-2018 under grant agreement No 633053. The views and opinions expressed herein do not necessarily reflect those of the European Commission.

Appendix

In this section we describe the video digitization and distribution, the real time processing system as well as real time processing algorithm

Video digitization and distribution

A data flow diagram which includes fundamental hardware components is shown in Fig.A1. The analogue composite video signal from the camera is digitised by a Gigabit Ethernet (GigE)



A.1 Video digitization and distribution synoptic.

frame grabber iPORT PT1000-ANL (2-6-V2-E). The frame grabber takes a composite video feed and generates a stream of packets of video data on a GigE network connection and sends the video data using networking technology to three separate destinations simultaneously [52]: the Real Time Processing System, a Video Capture and replay system for data storage, and the systems running the live displays. This setup is replicated for each Hitachi camera.

The iPORT is also capable, in conjunction with a suitable network switch, of sending its data to multiple destinations without sending duplicate frames of data to each. The iPORT internal clock (resolution 400ns) is reset by a trigger from the JET-ILW Control and Data Acquisition System (CODAS) at the start of the JET pulse (defined here as the point at which the central trigger and timestamp source is reset to zero, known at JET as the timing mark PRE). The data

packets it generates include this timestamp – and this is used by the video capture and real time systems to record a common time vector.

The real time processing system

The Real Time Processing System has been divided into a ‘Real Time Processing Unit’ (RTPU), for surface temperature calculation, and a ‘RTPU Host’, for connection between RTPU and other systems. The RTPU host is based on a standard industrial PC with Windows Embedded operating system. As shown in figure A2, the choice has been made to manage 2 RTPU within one JET-ILW standard industrial PC. Thus one standard PC manages 2 cameras. Additional details can be found in [53].

The cameras act as temperature sensors: pixel intensities are converted to temperatures. Each camera monitors multiple regions of interest (ROIs) for their maximum temperature. The system has to be capable of handling a maximum of 96 ROIs per camera. A real time processing unit (RTPU) for each camera calculates the temperature and sends the result across JET-ILW’s

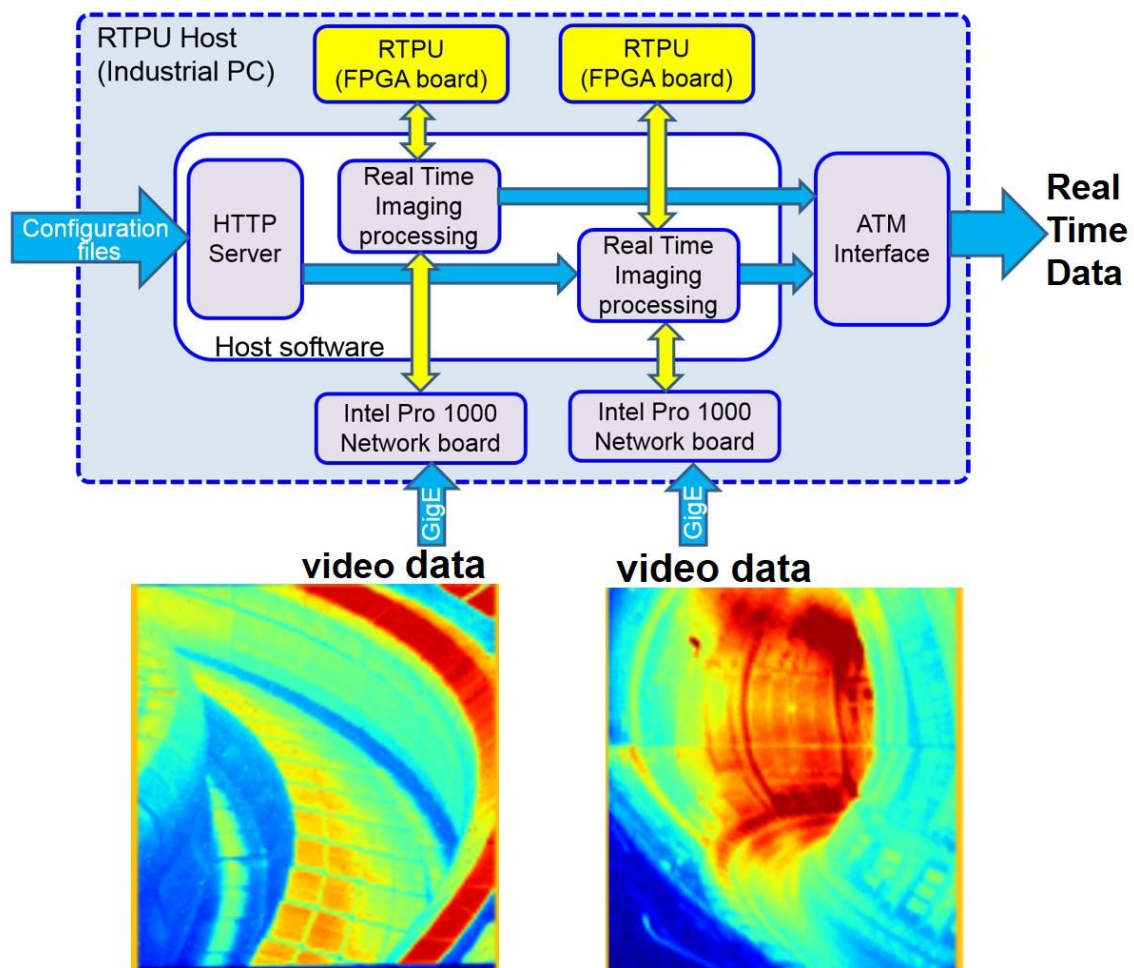


Fig.A2 The Real Time Processing Unit on JET-ILW.

Real Time Data Network (RTDN) to a separate real time system, the Vessel Thermal Map (VTM) [54,55]. The VTM assimilates all temperature inputs and, using the knowledge of how camera ROIs map to physical components, identifies events. If the temperature from an active ROI of some camera exceeds an alarm threshold, the VTM translates this to a ‘Main chamber Hot Spot’ or a ‘Divertor Hot Spot’ depending on where the event happens. Events are communicated to the Real Time Protection Sequencer (RTPS), which decides how the control actuators should respond. The response of the RTPS is programmable. The response action is usually *not* to stop something immediately, but to try a controlled plasma termination, called ‘soft landing,’ to reduce the risk of a disruption.

The overall system, from the ROIs to the responses, is highly configurable. The tool that does all this configuration at JET-ILW –and ensures that it is both consistent and audited– is called ‘Level1’.

The main functions of the Real Time Processing System are:

- Capture the camera data from Pleora iPORT modules with Intel Pro 1000 network boards and send them to RTPUs through the PCIe bus
- Receive all the configuration files and values from the JET-ILW Database and “Level-1”, then send them to the RTPUs through the PCIe bus. The configuration data are the ROI map, the dead pixel map, the Non Uniformity Correction matrix (offset and gain correction) and the calibration files that are Lookup Tables, which can manage a maximum of 6 different materials and/or optical transmissions (only 3 are currently in use: Beryllium, Tungsten and Tungsten coating)
- Collect results (maximum temperature values for each ROI...) from RTPUs and send them through the JET-ILW Real Time Data Network to the Vessel Thermal Map (VTM) [53]
- Handle the central timing for synchronisation with JET-ILW pulses
- Allow ROI display for proper positioning check

Real time processing algorithm

The RTPU is a field programmable gate array (FPGA) board that performs the real time image processing. The chosen FPGA board is a Sundance Multiprocessor PCI express SMT122T FX70T board, with the following main features: 4 lane PCI express interface, 1 FPGA Xilinx Virtex5 FX70T FGG665, 2 DDR2 memory banks (256Mbytes per bank), 1 Serial PROM 64Mbit, 2 Marvell 10/100/1000 Ethernet PHYs.

The main functions of the real time processing algorithm are:

- to evaluate the temperatures of multiple ROIs on each image of the video stream.
Each region of interest outputs three signals: the validated maximum temperature and the pixel coordinates (x,y) which correspond to the position of the hot spot.
- to ignore ‘dead’ pixels with artificially high or low intensity
- to apply a median filter and a per-pixel correction for sensor irregularities. False hot spots due to neutron hits on the sensor are discarded by using a median filter. The other ‘false’ hot spots, for example due to dust deposits, are eliminated by using a selection algorithm. This algorithm ignores hot spots that are too small. A dynamic ROI of 5×5 pixels is defined around the hottest pixel. If the minimum number of pixels, N_{pix} , is found to be above a threshold (in percent of the value of the hottest pixel), the hot spot is considered as valid. If not, the next hottest spot is selected and the validation process is repeated. N_{pix} and the threshold are configurable parameters. Typically $N_{pix} = 5$ and a threshold of 90% is used.
- to convert the measured intensity into temperatures using a look-up table for the material observed by the ROI.

JUVIL Video imaging software

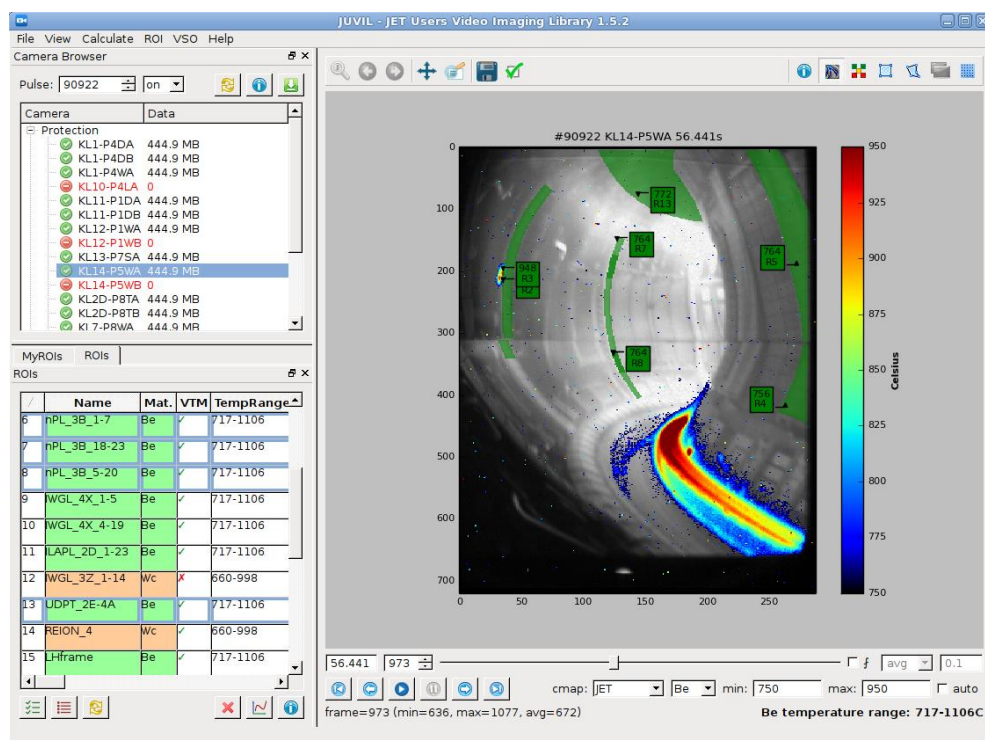


Fig.A3 JUVIL graphical Interface.

The JUVIL framework consists of modular object-oriented components written in *Python*. They provide standard interfaces to access video data and post-processing, are highly configurable and can be easily extended and adapted for new imaging cameras, data formats or developing applications for users' own analysis. Fig. A3 shows the JUVIL graphical interface. There is a separation between standard interfaces and site-specific implementations, e.g. JET-ILW specifics are implemented in a *jet* package. Such an object-oriented hierarchical structure provides a very efficient common platform with the possibility to reuse the functionality of existing components without the need to copy the code several times and facilitates the software maintenance. To convert the digital level counts of camera pixels into the real temperatures for a specific material, JUVIL subtracts the stored video background, loads the calibration file and performs dead pixels and flat field corrections.

References

- [1] Matthews G. F. *et al* 2011 *Phys. Scr.* **T145** 014001
- [2] Horton L. *et al* 2013 *Fusion Engineering and Design* **88** 434– 439
- [3] Maier H. *et al* *Phys. Scr.* 2009 **T138** 014031
- [4] Thomser C. *et al* 2012 *Fusion Science and Technology Volume* **62** 1-8
- [5] Mertens Ph. *et al* 2009 *Phys. Scr.* **T138** 014032
- [6] Herrmann A. 1996 *Optical surface temperature measurement*, in: P.E. Stott, G. Gorini, E. Sindoni (Eds.) *Diagnostics for Experimental Thermonuclear Fusion Reactors*, Plenum Press, New York and London
- [7] Herrmann A. *et al* 2011 *Fusion Eng. Des.* Volume **86** Issues 6–8 530–534,
<http://doi.org/10.1016/j.fusengdes.2011.02.037>
- [8] Coenen J.W. *et al* 2013 *Nucl. Fusion* **53** 073043 (8pp)
- [9] Summers H.P. *Atomic Data and Analysis Structure*, URL: <http://www.adas.ac.uk/>
- [10] Ramsey A. T. and Turner S. L. 1987 *Rev. Sci. Instrum.* **58** 1211
- [11] Meigs A *et al* 2010 *Rev. Sci. Instrum.*, 81 (10)10E532
- [12] CRC Handbook of Chemistry and Physics, 75th ed., edited by D. R. Lide and H. P. R. Frederikse (CRC, 1994).
- [13] Ruset C. *et al* 2012 “Advanced calibration of the PIW IR camera,” JET Progress Report, JW10-TA-PIW-ACIR-02
- [14] Thomas L.K. 1968 *Journal of Applied Physics* 39 4681-4686.
- [15] Widdowson A. private communication
- [16] Huber A. *et al* 2017 *Fusion Eng. Des.* Volume **123** 669-673,
<http://dx.doi.org/10.1016/j.fusengdes.2017.03.167>

- [17] S. J. Sangwine and R.E.N.Horne, The Colour Image Processing Handbook, Springer, Boston, MA, ISBN 978-1-4615-5779-1, <http://dx.doi.org/10.1007/978-1-4615-5779-1>.
- [18] http://www.eureca.de/english/optoelectronics_sony.html
- [19] Sieglin B. *et al* 2013 Plasma Phys. Contr. Fusion **55** 124039, doi:10.1088/0741-3335/55/12/124039
- [20] Eich T. *et al* 2011 Phys. Rev. Lett. **106** 215001
- [21] Hirai T. *et al* 2007 "Characterization and heat flux testing of beryllium coatings on Inconel for JET ITER-like wall project" *Phys. Scr.* **T128** 166.
- [22] Coenen J.W. *et al* 2015 *J. Nucl Mater* **463** 78-84, <https://doi.org/10.1016/j.jnucmat.2014.08.062>
- [23] Nachtigall E. 1955 *Der Ablauf der Rekristallisation bei Molybdän und Wolfram* 2. Plansee-Seminar 'De re metallica' Reutte, Austria—in *Chem. Ingenieur Tech.* **27** (2004) 794
- [24] Huber A. 2014 *et al.* Phys. Scr. **T159** 014005
- [25] Riccardo V. *et al* 2005 *Nucl. Fusion* **45** 1427
- [26] Huber A. *et al* 2012 *Rev. Sci. Instrum.* **83** 10D511
- [27] Huber A. *et al* 2013 *Fusion Engineering and Design* **88** 1361– 1365
- [28] Litnovsky A. *et al* 2007 *Nucl. Fusion* **47** 833–838
- [29] Mertens Ph. *et al* 2015 *Fusion Engineering and Design* **96–97** 129–135
- [30] Marot L. *et al* 2007 *Rev. Sci. Instrum.* **78** 103507, <http://dx.doi.org/10.1063/1.2800779>
- [31] Marot L. *et al* 2008 *Surf. Sci.* **602** 3375-3380, <http://dx.doi.org/10.1016/j.susc.2008.09.012>
- [32] Marot L. *et al* 2009 *J. Nucl. Mater.* **390-391** 1135, <http://dx.doi.org/10.1016/j.jnucmat.2009.01.266>
- [33] Clever M. *et al* 2013 *Fusion Eng Des* **88** 1342-1346, <http://dx.doi.org/10.1016/j.fusengdes.2013.01.038>
- [34] Marot L. *et al* 2015 *Journal of Coating Science and Technology* **2** 72-78
- [35] Arnoux G. *et al* 2012 *Rev. Sci. Instrum.* **83** 10D727
- [36] Biewer T. M. *et al* 2012 *Rev. Sci. Instrum.* **83** 10D505
- [37] Huber V. *et al* 2016 *Rev. Sci. Instrum.* **87** 11D430, doi: 10.1063/1.4959912
- [38] Balboa I. *et al* 2016 *Rev. Sci. Instrum.* **87** 11D419
- [39] B. Lipschultz *et al* 1984 *Nucl. Fusion* **24** 977
- [40] Huber V. *et al* 2017 *Fusion Eng. Des.* **123** 979-985, <http://dx.doi.org/10.1016/j.fusengdes.2017.03.005>

- [41] Brezinsek S. *et al* 2015 *J. Nucl. Mater.* **463** 11,
<https://doi.org/10.1016/j.jnucmat.2014.12.007>
- [42] M. Mayer *et al* *Phys. Scr.* **T170** (2017) 014058.
- [43] M. Tokitani *et al* *Fusion Eng. Des.* <https://doi.org/10.1016/j.fusengdes.2018.01.051>
- [44] Widdowson A. *et al* 2017 *Nuclear Materials and Energy* **12** 499-505,
<http://dx.doi.org/10.1016/j.nme.2016.12.008>
- [45] Maier H. *et al* 2016 *Phys. Scr.* **T167** 014048. <http://dx.doi.org/10.1088/0031-8949/T167/1/014048> .
- [46] Hermann A. 2002 *Plasma Phys. Contr. Fusion* **44** 883
- [47] Joffrin E. *et al* 2017 *Nucl. Fusion* **57** 086025
- [48] Widdowson A. *et al* 2017 *Nucl. Fusion* **57** 086045 (9pp), <https://doi.org/10.1088/1741-4326/aa7475>
- [49] Catarino N. *et al* 2017 *Nucl. Mater. Energy* **12** 559-563
(<https://doi.org/10.1016/j.nme.2016.10.027>)
- [50] Mayer M. *et al* 2016 *Phys. Scr.* **T167** 014051
- [51] Petersson P. *et al* 2015 *J. Nucl. Mater.* **463** 814
- [52] Kinna D. 2010 *JET CDN Report H(10)007*
- [53] Jouve M. *et al* 2011 *Real-time protection of the ITER-like wall at JET*, in: Proc.13th Int. Conf. on Accelerator and Large Experimental Physics Control Systems, Grenoble
- [54] Stephen A. *et al* 2012 *Phys. Rev. ST Accel. Beams* **15** 054701
- [55] Alves D. *et al* 2012 *Phys. Rev. ST Accel. Beams* **15** 054701